Continuum Effective-Stress Approach for High-Rate Plastic Deformation of Fluid-Saturated Geomaterials with Application to Shaped-Charge Jet Penetration

Michael A. Homel, James Guilkey, Rebecca M. Brannon[a,b,c,]

[a] *University of Utah, Department of Mechanical Engineering*
[b] *University of Utah, Department of Mechanical Engineering*
[c] *The University of Utah, Department of Mechanical Engineering, 50 S. Central Campus Dr., MEB 2110, Salt Lake City, Utah 84112*

Abstract

A practical engineering approach is presented for modeling the constitutive response of fluid-saturated porous geomaterials under loading that is typical of shaped-charge jet penetration for wellbore completion. An analytical model of a saturated thick spherical shell provides valuable insight into the qualitative character of the elastic-plastic response with an evolving pore fluid pressure. However, intrinsic limitations of such a simplistic theory are discussed to motivate the more realistic semi-empirical model used in this work. The constitutive model is implemented into a material point method (MPM) code that can accommodate extremely large deformations. Consistent with experimental observations, the simulations of wellbore perforation exhibit appropriate dependencies of depth of penetration (DOP) on pore pressure and confining stress.

Keywords: effective stress, geomaterial, plasticity, backstress, high-rate, shaped-charge jet, porous, fluid saturated, spherical shell, material point method

1. Introduction

1.1. Fluid Saturated Porous Materials

Deformation characteristics of fluid-saturated porous materials are fundamental to geomechanics modeling (Karrech et al., 2012), with conventional engineering applications in hydrogeology, biomechanics, and ceramic processing (Wang, 2000), as well as emerging applications in biomechanics, such as simulating bone regrowth (Swan et al., 2003; Kohles et al., 2002; Borja, 2006; Gupta et al., 2007), ice flow and climate modeling (Scambos et al., 2000; Kamb, 1991). For high-rate, large-deformation simulations, it is necessary to model not only the elastic response, but also the response to inelastic deformation such as pore collapse and the loss of strength due to the introduction of microcracks or voids (Strack et al., 2014). In continuum approaches, homogenization is applied so the two-phase material can be represented as a mechanically-equivalent single phase (Geiser; and Blight, 2004), which (as can be confirmed via mesoscale modeling at various strain rates) is a reasonable approximation for high-rate applications such as wellbore completion.

1.2. Effective-Stress Model History

Modern approaches for continuum modeling of fluid-saturated porous media define an "effective stress," first introduced by Terzaghi (1936) and Fillunger (1915) that governs the stress-strain response and strength of a porous material (Schrefler and Gawin, 1996). The general formulation for effective stress is

$$\sigma^{\text{eff}} \equiv \sigma - \alpha \overline{p}_f \mathbf{I}, \tag{1}$$

where $\overline{p}_f$[1] is the pore fluid pressure, and α is Biot's parameter (Schrefler and Gawin, 1996; Biot, 1956, 1941). The appeal of the effective-stress approach is that it allows the response of a porous solid with fluid pressure to be determined from the measured response of a drained sample (Nedjar, 2012), for which experimental methods are more tractable (Nur and Byerlee, 1971). While the effective-stress concept has been extended to partially-saturated material to describe effects of matric suction (Sun et al., 2007) and molecular adhesion (Anandarajah, 2010), studies on the capillary stress tensor in wet granular materials have shown the pore fluid in unsaturated material is "inherently anisotropic and strongly dependent on the combined loading and hydric history of the material" (Scholts et al., 2009) making it fundamentally different from an isotropic fluid pressure and thus calling into question the applicability of the effective-stress approach for unsaturated granular materials (Xie and Shao, 2012; Sheng et al., 2013). At sufficiently-high strain rates fluid transport through the pore network can be neglected (Nedjar, 2013), so this discussion will focus on the case of a fully-saturated material with a pore fluid pressure that evolves with local material deformation.

1.2.1. Elastic Response

The elastic response of a porous material with pore pressure can be expressed in terms of an effective stress (Wang, 2000). For linear-elastic deformation, where the pore pressure is assumed to be proportional to strain, a theoretical value for Biot's

[1] Throughout this manuscript, an overbar denotes a quantity that is positive in compression.

parameter is (Schrefler and Gawin, 1996)

$$\alpha = 1 - \frac{K}{K_s'}, \tag{2}$$

where K and K_s' are the bulk moduli of the drained and undrained porous material, respectively. This definition is consistent with experimental evidence and provides the correct response in the limit as porosity goes to zero (Nur and Byerlee, 1971).

1.2.2. Inelastic Response

Terzaghi's effective-stress postulate agrees well with experimental data for soils and rock materials under the stresses typical of geotechnical applications, but the strength properties at very high stresses cannot be determined accurately without accounting for micromechanical considerations (Jaegar and Cook, 1976; Goodman, 1980; Buhan and Dormieux, 1996; Schrefler and Gawin, 1996; Barthelemy and Dormieux, 2010). While the poroelastic effective-stress model can be derived theoretically (Coussy, 1995) asserts that there is no similar justification for evaluating the material strength based on effective stress. Accordingly, the stress and fluid pressure must be accounted for independently in the yield function, $f'(\sigma, \overline{p}_f)$, which cannot be determined directly from the yield function for the drained material, $f(\sigma)$. Buhan and Dormieux (1996) show that an effective-stress approach *is* applicable when the matrix strength depends only on the stress deviator (e.g., von Mises or Tresca yield conditions), and they conclude that the approach represents a "safe lower bound" for materials with frictional strength properties (e.g., Mohr-Coulomb or Drucker-Prager yield conditions) with a vertex at the origin of stress space; experimental investigations support this assertion for specific low-rate (Xie and Shao, 2012) and high-rate (Lomov et al., 2001) load cases, but the subject remains an open research topic (Xie and Shao, 2012; Wilmanski, 2006).

1.3. Shaped-Charge Jet Penetration

High-rate constitutive modeling of saturated porous materials is crucial to any computational investigation of wellbore completion, in which a shaped-charge jet is used to penetrate the well casing and surrounding rock in order to open a pathway for oil to flow. A well-known guideline for shaped charge jet explosives correlates the depth of penetration (DOP) to the ratio of densities of the penetrator to the target (Cooper, 2007). However, it is widely observed that the penetration depth is greater into undrained rock than into drained, despite the increased target density, emphasizing the need to better understand the role that a pore space fluid plays in the material response (Grove et al., 2008).

Simulation of shaped-charge jet penetration into rock is highly nontrivial, with large deformation, large rotation, multiple materials and contact that would require adaptive remeshing to avoid mesh entanglement in traditional finite element methods (Lee and Bathe, 1994). The need for an accurate constitutive response of the target materials precludes Eulerian approaches (Antoun et al., 2006) that do not allow for full-stress constitutive models with history-dependent properties (Liu et al., 1986). A promising alternative is the material point method (MPM), which is a mixed Eulerian-Lagrangian approach that solves the equations of motion on a fixed background grid while tracking the material state on particles that travel through this grid (Bardenhagen et al., 2000). The penetration simulations and mesoscale modeling described herein are performed in Uintah, a scalable parallel environment for multiphysics simulations that includes capabilities for various implementations of the material point method, as well as support for explosives and fluid-structure interactions (Guilkey et al., 2009).

2. Methods

We will describe first an analytical model for a thick spherical shell that contains a pore fluid. This idealized model is not directly applicable to constitutive modeling of geomaterials, but does provide valuable insight into the desired elastic-plastic response with an evolving pore fluid pressure. A practical empirically based solution method is then presented to mitigate some errors in the shell model associated with the clearly unrealistic morphology and to accommodate a generalized effective-stress principle for elastic-plastic deformation under arbitrary loading. Finally we describe the application of this model to MPM simulations of wellbore completion, to produce experimentally observed trends in penetration channel formation vs. pore pressure and confining stress.

2.1. Analytical Model of a Thick Spherical Shell

To better understand the effect of a pore fluid on the constitutive response of a porous material, we first consider the idealized case of a linear-elastic, perfectly-plastic, incompressible, thick spherical shell, for which analytical solutions can be derived to describe the response to hydrostatic loading. This classical starting point was presented by Carroll and Holt (1972), who derived an analytical solution for the pressure during pore collapse in three regions, (i) fully elastic, (ii) elastic-plastic, and (iii) fully-plastic, as a function of the current and initial distension (ratio of the density of the matrix and bulk materials), the

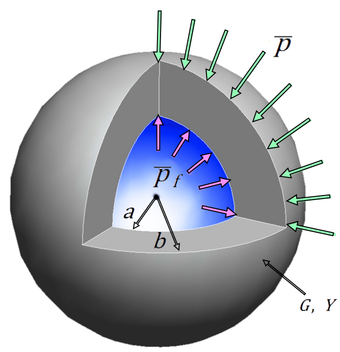

Figure 1: Diagram of the thick spherical shell with a pore fluid pressure. The shell material is linear-elastic, perfectly plastic, and incompressible so the porosity depends only on the displacement of the outer surface.

shear modulus (G) and the yield strength (Y) of the shell material. Extending their work to include an evolving fluid pressure at the pore surface, we prove in Appendix A that Terzhagi's postulate (Buhan and Dormieux, 1996) is valid for this system, and the resulting steady-state solution can be expressed in terms of an "effective pressure," defined as the difference in pressure at the inner and outer surface.

2.1.1. Response

The porosity vs. pressure responses of the hollow and fluid-filled spherical shells are plotted in Fig. 2. For the hollow shell, the compressive fully plastic response (i.e., the orange "crush" curve on the right-hand side of the figure) is independent of the initial porosity, but for the fluid-filled shell the pore pressure – and thus the overall response – depend on the initial pore volume.

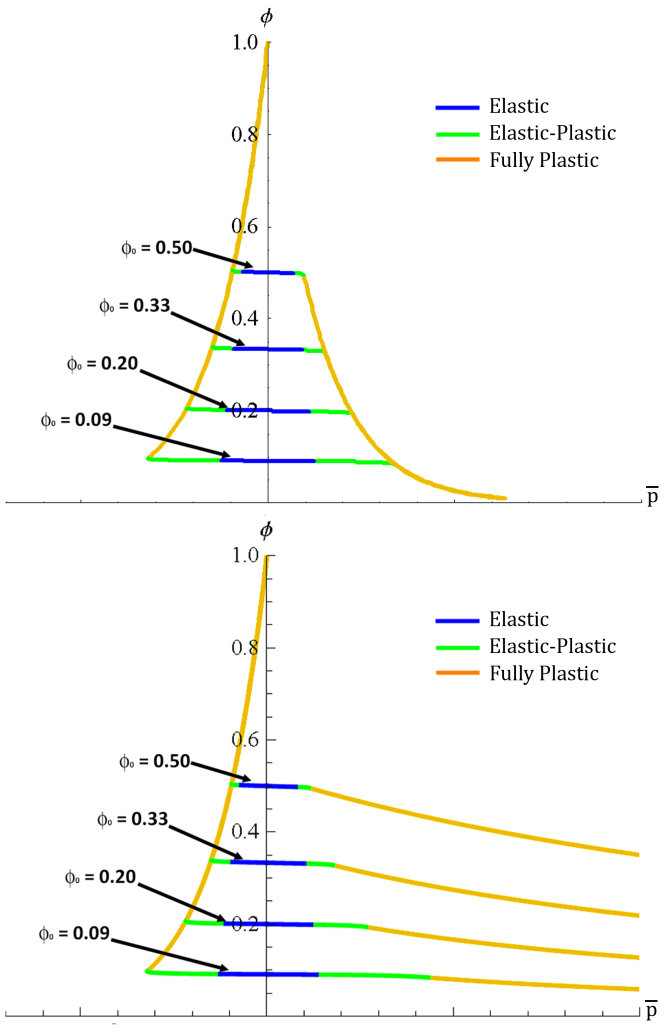

Figure 2: Porosity vs. pressure for a hollow (top) and fluid-filled (bottom) thick spherical shell, for a range of initial porosities

In spherical tension, the elastic-plastic to fully-plastic transition occurs at a lower stress as dilatation increases, an unstable response resulting from thinning of the spherical shell. An interesting result is observed when plotting the tensile response for very low initial porosities, in which the shell thinning occurs in the elastic-plastic domain as shown in Fig. 3. For such cases, there exists a region of unrealizable states, enclosed by the fully plastic envelope, that cannot be achieved through quasistatic deformation. While not directly relevant to the effective-stress development, this has important implications as a potential pore nucleation criterion in spherical tension.

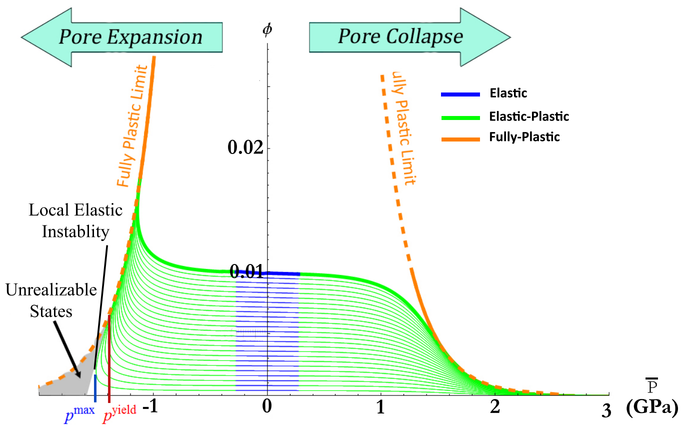

Figure 3: Pore collapse and expansion for a hollow thick spherical shell for a range of low initial porosities

2.1.2. Continuum Implementation

Using the analytical solution for the fluid-filled spherical shell from Appendix A , the load-unload response of the spherical shell is computed, as shown in Fig. 4. During decompression, accumulated fluid pressure causes the matrix material to expand beyond its zero effective-stress state, inducing yield in biaxial tension within the matrix material while the confining pressure remains spherical and compressive. As a result, the matrix material undergoes significant extensional plastic strain during unloading, and is in a state of incipient tensile yield at the unloaded equilibrium. This mechanism could affect the damage (de Borst et al., 1999) and therefore the permeability (Morris et al., 2003) in the deformed structure. From the analytical solution to the spherical shell, expressions can be derived for the evolution of the hydrostatic compressive strength and the unloaded fluid pressure with volumetric plastic strain. The accumulated fluid pressure creates a hydrostatic shift (ζ) in the yield surface, interpreted as an isotropic backstress, and pore collapse evolves the hydrostatic compressive strength (X), herein defined as the value of the first stress invariant (I_1) at the elastic limit. Both X and ζ evolve with plastic strain as illustrated in Fig. 5.

While it is possible to obtain a set of evolution equations for X and ζ from the spherical shell model, direct continuum implementation of these equations is problematic. The response of a ductile spherical shell is a poor approximation for the nonlinear response of a geomaterial, and the approximation error is not significantly reduced by treating the model parameters as empirical fitting parameters. More critically, the analytical solution is tractable only because it assumes an incompressible

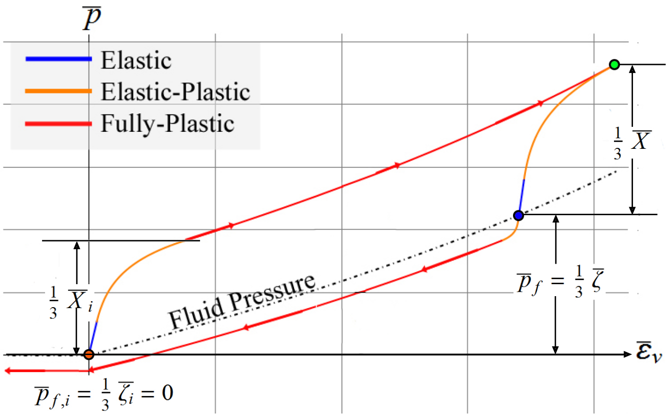

Figure 4: Load/unload response for an incompressible thick spherical shell with compressible pore fluid. The dots correspond to the states indicated in Fig. 5.

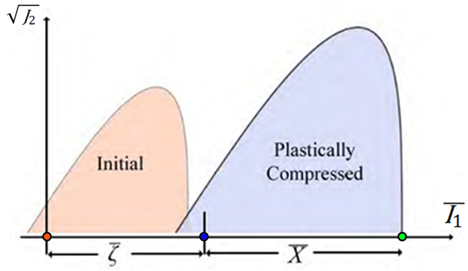

Figure 5: Evolution of constitutive model state variables for the hydrostatic compressive strength (X) and the isotropic backstress (ζ) for some compressive increment in volumetric plastic strain.

matrix, so that the pore volume is a simple function of the bulk volumetric strain. Without this assumption it becomes very difficult to define the boundary conditions at the pore surface during plastic deformation, but with this assumption the model becomes overly stiff in the limit of low porosity, and only allows a finite compressive strain.

2.2. *Empirical Approach Model*

A new approach was taken in this work to describe the hydrostatic constitutive response of the saturated material, which accounts for matrix compressibility while ensuring a consistent coupling between the models for elastic response, pore collapse, and evolution of the pore pressure.

Since classical poroelasticity is limited to linear elastic deformation (Karrech et al., 2012), we must derive an approximate relation to predict the porosity during pore collapse as a function of the compressibilities of the fluid and matrix phases.

2.2.1. *Isotropic Backstress Evolution*

We begin by assuming that the volume reduction in each phase is proportional to the applied pressure, so that each phase contributes a resistance to the overall change in volume that is a function of its volume fraction and bulk modulus.

The fluid is described by a simple logarithmic equation of state, so the fluid pressure ($\bar{p}_f$) is a function of the fluid bulk modulus (K_f), and the change in fluid volume (V_f) from the initial state (V_f^i), and possibly the additional zero-strain fluid pressure ($\bar{p}_f^i$),

$$\bar{p}_f = K_f \ln\left(\frac{V_f^i}{V_f}\right) + \bar{p}_f^i. \tag{3}$$

Neglecting grain-scale heterogeneity and assuming the overall effective response of the matrix is isotropic, we express the change in matrix volume (V_m) from the initial state ($V_m^i = (1-\phi_i)V_{\text{tot}}^i$) in terms of an effective matrix pressure ($\bar{p}_m$) and bulk modulus (K_m):

$$\bar{p}_m = K_m \ln\left(\frac{V_m^i}{V_m}\right) \tag{4}$$

The initial porosity (ϕ_i) is defined as

$$\phi_i = \frac{V_f^i}{V_m^i + V_f^i}. \tag{5}$$

Volumetric strain (ε_v) is defined as a sum of elastic (ε_v^e) and plastic (ε_v^p) strains, based on the total volume change from an initial unit volume:

$$\varepsilon_v = \ln\left(\frac{V_f + V_m}{V_f^i + V_m^i}\right). \tag{6}$$

Combining Eq. 3 through Eq. 6 gives

$$\phi_i\, e^{\bar{p}_m/K_m} = \mathrm{e}^{(\bar{p}_f - \bar{p}_f^i)/K_f}\left(e^{\varepsilon_v + \bar{p}_m/K_m} + \phi_i - 1\right). \tag{7}$$

Consider a material that has been compressed plastically and unloaded to a point of zero effective stress ($\bar{p}^{\text{eff}} = \bar{p} - \bar{p}_f = 0$), such as the state corresponding to the blue dot in Fig. 4. At this point, the stress coincides with the shifted elastic center, which implies zero elastic strain in an effective stress framework. The plastic strain therefore then equals the total strain $\varepsilon_v = \varepsilon_v^p$. For some control volume, the boundary of the matrix material is subject to either the fluid pressure or the confining pressure, as shown in Fig. 6. For a homogenized matrix material, the deformation is self similar, and the effective matrix pressure must equal that of the fluid and confinement ($\bar{p}_m = \bar{p}_f = \bar{p}$). This homogenization neglects variations in residual stress throughout the matrix material, but is used only to estimate the total compressed matrix volume. To account for heterogeneity, the effective matrix bulk modulus (K_m) should be determined directly from measurements of the drained material once all porosity has been crushed out, rather than from theoretical properties of a single grain or crystal. Equation 7 can now be applied to relate the pressure ($\bar{p}$) and volumetric plastic strain (ε_v^p).

$$\phi_i\, e^{\bar{p}/K_m} = e^{(\bar{p} - \bar{p}_f^i)/K_f}\left(\mathrm{e}^{\varepsilon_v^p + \bar{p}/K_m} + \phi_i - 1\right) \tag{8}$$

In this unloaded, plastically deformed state, the pressure is proportional to the isotropic backstress shift of the yield surface $\zeta = -3\bar{p}_f = -3\bar{p}(\varepsilon_v^p)$. While Eq. 8 cannot be solved explicitly for $\bar{p}(\varepsilon_v^p)$, implicit differentiation can be used to obtain an evolution equation for the isotropic backstress:

$$\left(\frac{\partial \zeta}{\partial \varepsilon_v^p}\right) = \frac{3K_f K_m\, e^{\varepsilon_v^p}}{\left(K_f + K_m\right) e^{\varepsilon_v^p} - \phi_i K_f\, e^{\frac{3\bar{p}_f^i + \zeta}{3K_f}} - (1-\phi_i)\, K_m\, e^{\frac{\zeta}{3K_m}}}. \tag{9}$$

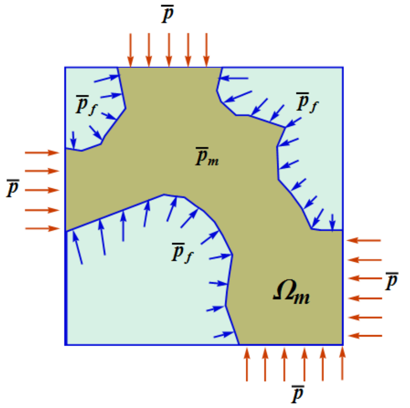

Figure 6: RVE schematic of the pressure acting on the matrix domain for the special case of zero effective stress so the pressure ($\bar{p}$) equals the fluid pressure ($\overline{p}_f$).

2.2.2. *Porosity-Strain Relationship*

Eq. 9 describes the evolution of the unloaded pore pressure with plastic deformation, but to estimate the change in elastic properties with deformation, it is also necessary to derive a porosity-strain relationship.

In terms of an engineering strain measure, the total volumetric strain (ε_v) can be defined in terms of the volumetric strain in each phase and the initial porosity as

$$\varepsilon_v = \phi_i\, \varepsilon_v^f + (1-\phi_i)\varepsilon_v^m. \tag{10}$$

Approximating the pressure in each phase as equal ($-\varepsilon_v^f K_f + \bar{p}_f^i = -\varepsilon_v^m K_m$), and solving Eq. 10 for the volumetric strain in each phase,

$$\varepsilon_v^f = \frac{\varepsilon_v K_m + (1-\phi_i)\bar{p}_f^i}{(1-\phi_i)K_f + \phi_i K_m}. \tag{11}$$

$$\varepsilon_v^m = \frac{\varepsilon_v K_f - \phi_i \bar{p}_f^i}{(1-\phi_i)K_f + \phi_i K_m} \tag{12}$$

Eq. 10 comes from the following four equations:

$$\varepsilon_v^f = \frac{V_f - V_f^i}{V_f^i} \tag{13}$$

$$\varepsilon_v^m = \frac{V_m - V_m^i}{V_m^i} \tag{14}$$

$$\varepsilon_v = \frac{V_f + V_m - (V_f^i + V_m^i)}{V_f^i + V_m^i} \tag{15}$$

$$\frac{V_f^i}{V_f^i + V_m^i} = \phi_i. \tag{16}$$

These equations assume an engineering strain measure. For logarithmic (Hencky) strain measure, the relation (analogous to Eq. 10) is

$$e^{\varepsilon_v} = e^{\varepsilon_v^m}(1-\phi_i) + e^{\varepsilon_v^f}\phi_i. \tag{17}$$

This form is not used because no algebraic solution exists (analogous to Eq. 11 and Eq. 12) when using the logarithmic strain measure. Although an engineering strain measure introduces error when applied to large-deformations, here we are only determining the relative volume change of the two phases, which mitigates this error.

Combining Eq. 11 and Eq. 12 gives the following approximate relationship between the current porosity and the total volumetric strain:

$$\phi(\varepsilon_v) = \frac{\phi_i\ e^{(\bar{p}_f^i + K_m\varepsilon_v)/\chi}}{\phi_i\ e^{(\bar{p}_f^i + K_m\varepsilon_v)/\chi} + (1-\phi_i)\, e^{K_f\varepsilon_v/\chi}} \tag{18}$$

where

$$\chi = K_f\,(1-\phi_i) + \phi_i K_m. \tag{19}$$

This expression is only an approximation, since the actual pore pressure would depend on the path-dependent residual stress state in the matrix material.

2.2.3. *Bulk Modulus*

The elastic tangent bulk modulus of the saturated material K_s' can be estimated using the classical approach presented by Biot (1941) and Gassmann (1951) based on the bulk modulus of the drained material (K), the material porosity (ϕ), and the bulk moduli of the fluid (K_f) and solid (K_m) phases.

$$K_s' = K + \frac{\gamma^2}{\frac{\gamma}{K_m} + \phi\left(\frac{1}{K_f} - \frac{1}{K_m}\right)},\ \text{where } \gamma = 1 - K/K_m \tag{20}$$

Hart and Wang (1995) demonstrated that this formulation produces a reasonable approximation for the measured hydrostatic properties of Berea sandstone and Salem limestone up to the elastic limit. In extending this model to large deformation, we allow the porosity to depend on plastic strain according to Eq. 18, with the drained bulk modulus varying according to Eq. 21.

While it may be possible to improve the predictions with models that account for micromechanical considerations (*c.f.,* Pietruszczak and Pande (1995)) (most importantly that the solid phase in typical sedimentary rock is inhomogeneous), the improved models require either additional experimental measurements, or knowledge of the microstructure that may not be readily obtainable. In contrast, the present approach requires only measurements that can be obtained directly from the hydrostatic response of the bulk material.

These poroelasticity approaches are derived under the assumption of quasistatic deformation, so that a state of purely isotropic stress can be assumed to exist throughout the pore fluid. This assumption loses validity at higher rates of loading, where local shear stresses would no doubt exist (even in a macroscopic hydrostatic loading) as the pore space deformed. The magnitude of the shear stresses for a given load path would depend additionally on the strain rate and viscosity of the fluid, but the amount of shear deformation in the fluid would depend on the microstructure and could likely not be inferred from quasistatic hydrostatic data. This is one of several dynamic effects that are accommodated *en ensemble* with a Duvaut-Lion rate dependent model.

2.2.4. *Parameterization*

The hydrostatic load-unload response of a drained material is well described by empirical formulations. The elastic tangent bulk modulus in compression can be approximated as a function of the hydrostatic stress (I_1), volumetric plastic strain (ε_v^p), and parameters (b_i) by the relation (Brannon et al., 2009):

$$K = b_0 + b_1\ e^{-b_2/|I_1|} - b_3\ e^{-b_4/|\varepsilon_v^p|}, \tag{21}$$

where b_0 is the initial value, and $b_0 + b_1$ is the high-pressure limit, which is assumed to be equal to the bulk modulus of the solid phase (K_m).

The crush curve, which defines the relation between the hydrostatic compressive strength (i.e., the evolving value, X, of the first stress invariant, I_1, beyond which pores irreversibly collapse in compression) and volumetric plastic strain is described by Brannon et al. (2009):

$$X(\varepsilon_v^p) = p_0 + \frac{1}{p_1}\ln\left(\frac{\varepsilon_v^p + p_3}{p_3}\right), \tag{22}$$

where p_0 is the value of I_1 at the initial hydrostatic compressive limit, p_1 is a shape parameter, and p_3 is the magnitude of the maximum achievable compressive volumetric plastic strain. The initial porosity is related to the crush curve parameters by

$$\phi_i = 1 - e^{-p_3}. \tag{23}$$

This development has used a simple one-parameter logarithmic equation of state for the fluid. The fluid bulk modulus is selected to best approximate the fluid response over the range of application. Figure 7 compares this logarithmic equation to the Tait equation (Li, 1967), for a wide range of pressure. A reduced value of the fluid bulk modulus could be used to roughly approximate the response of a partially saturated material. Though this neglects the effect of matric suction, it may be suitable for high-rate applications. The logarithmic equation of state was selected because it produces tractable analytical expressions for the state variable evolution, porosity, and fluid pressure. In principal the approach presented in this paper could be used with a more complex equation of state (or even a lookup table).

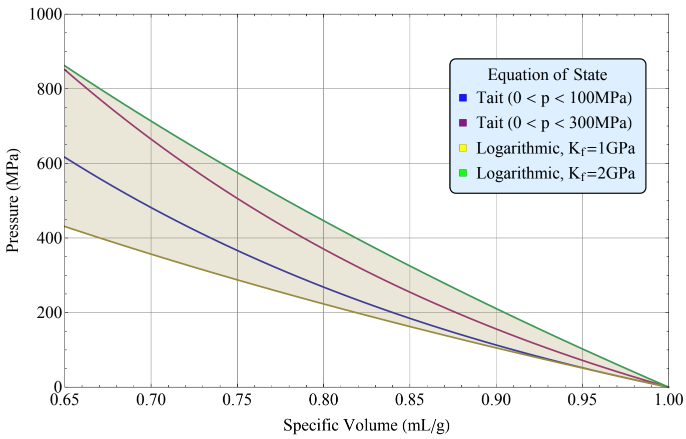

Figure 7: Comparison of the logarithmic equation of state with two values of bulk modulus to the Tait equation of state, fit to Amagat's data (Li, 1967) over two pressure ranges.

2.2.5. *Empirical Strain-to-Yield Model*

The model for the elastic tangent bulk modulus of a saturated material can be extended to obtain a crush curve equation for the undrained material using only the empirical characterization of the drained material.

Assuming the drained material is well-characterized by empirical relations, the following relationship exists between the hydrostatic strength (Eq. 22), elastic tangent bulk modulus (Eq. 21), and the volumetric strain-to-yield ($\varepsilon_v^{e,\text{yield}}$).

$$X(\varepsilon_v^p) = 3\int_0^{\varepsilon_v^{e,\text{yield}}} K\left(I_1, \varepsilon_v^p\right) d\varepsilon_v^{e,\text{yield}} \tag{24}$$

Using a midpoint rule to approximate the integral in Eq. 24, we evaluate Eq. 21 at the halfway point to yield ($I_1 \approx \frac{1}{2}X\left(\varepsilon_v^p\right)$), which gives a simple expression for the elastic volumetric strain-to-yield as a function of the volumetric plastic strain:

$$\varepsilon_v^{e,\text{yield}}(\varepsilon_v^p) = \frac{1}{3}\frac{X\left(\varepsilon_v^p\right)}{K\left(I_1 \varepsilon_v^p\right)} = \frac{\frac{1}{3}X\left(\varepsilon_v^p\right)}{b_0 + b_1\ e^{-2b_2/|X(\varepsilon_v^p)|} - b_3\ e^{-b_4/|\varepsilon_v^p|}}, \tag{25}$$

Assuming that the volumetric strain-to-yield ($\varepsilon_v^{e,\text{yield}}$) is the same for the drained and undrained materials, we can now use the semi-empirical formula for the bulk modulus of the saturated material (Eq. 21) to estimate the hydrostatic compressive yield stress for the saturated material:

$$\bar{X}'(\varepsilon_v^p) = 3K_s'\varepsilon_v^{e,\text{yield}}(\varepsilon_v^p) \tag{26}$$

The strain-to-yield approach, implicitly assumes that the matrix material strength does not depend on pressure, which is consistent with the theoretical limitations of the applicability of the effective-stress approach for plastic deformation described by Buhan and Dormieux (1996).

The matrix material for a porous rock would certainly have frictional strength properties, but in justifying this assumption, we suggest the following: During pore collapse the plastic deformation localizes near contact points between grains, where the surrounding pore pressure may act to both expand microcracks exposed to the pore fluid and to compress microcracks that are isolated from the pore space. These competing effects would mitigate the effect of matrix strength pressure dependence on the overall response. word this better In this paper we present results that show this approach can predict the correct trends in penetration simulations. This strain-to-yield approach has been motivated by mesoscale simulation that elucidate the grain-scale plastic deformation of saturated granular materials (Homel et al., 2014a).

2.3. *Simulation of Wellbore Completion*

To demonstrate the application of this effective-stress model, we simulate hypervelocity penetration into drained and undrained sandstone, with a variety of preconfinement and initial pore pressure states.

The simulations use the material point method (MPM) (Sulsky et al., 1995) component of the Uintah Computational Framework (Guilkey et al., 2009). Except where noted, the results are for 2-D axisymmetric simulations, and use a cpGIMP (Bardenhagen and Kober, 2004) form of the material point method. Previous work by Austin (2013) determined a suitable target domain, mesh resolution, particle density and method for ramped application of boundary conditions that mitigate edge effects on the simulation results.

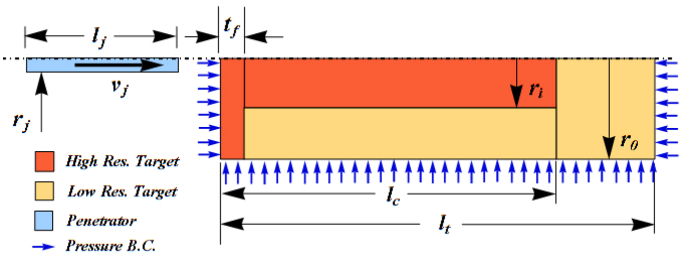

Figure 8: Diagram showing the problem setup for the axisymmetric penetration simulations.

2.3.1. Target Description

The target is a sandstone cylinder, with a radius 5cm, and a length sufficient to avoid interaction of the pressure pulse reflection from the cylinder end with the channel formation. In some cases, a steel plate is defined at the penetrator surface, to model the effect of the wellbore casing.

The constitutive model for the sandstone target is Arenisca (Homel et al., 2014b), an open-source geomaterial model developed by the authors to implement the effective-stress approach described herein.

The strength is defined by a two-surface description combining a shear limit surface and a porosity cap function, similar to those shown in Fig. 5. The shear strength is defined by a nonlinear Drucker-Prager surface, fit to data from plate-slap (Lomov et al., 2001), triaxial compression, unconfined compression, and tension tests (Bobich, 2005), as shown in Fig. 9. The elastic response supports nonlinear elasticity with elastic-plastic coupling for the bulk modulus (Eq. 21) (Brannon et al., 2009). The evolution of the porosity cap is defined in compression by the hydrostatic crush curve (Eq. 22), and in dilatation by an extension of this curve that introduces a loss of strength with pore expansion. The bulk modulus and crush curve functions are fit to hydrostatic load-unload data for Berea sandstone, shown in Fig. 10. The plastic solution allows for nonassociativity to control the shear-induced dilatation (Burghardt et al., 2012). A Duvaut-Lions viscoelasticity model describes the apparent increase in strength with increased strain rate (*c.f.,* (Simo and Hughes, 1998)).

In initializing the pore pressure and confining stress, a Neumann boundary condition is applied to the outer surfaces of the target; the pressure is ramped from the value of the initial pore pressure to that of the confining stress. This preload is done

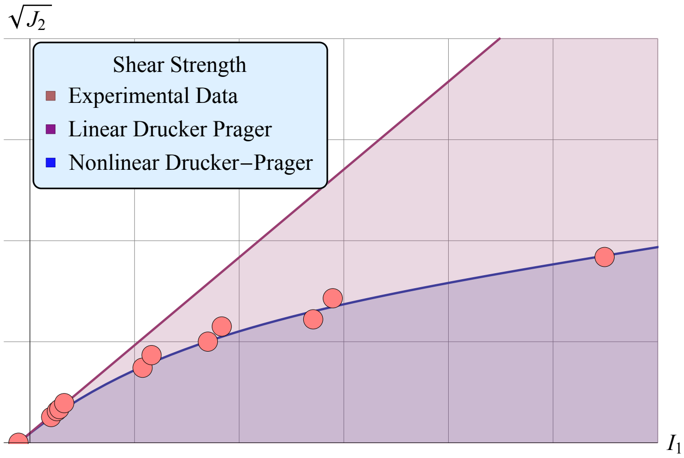

Figure 9: Parametrization of the nonlinear Drucker-Prager shear limit function to experimental data for Berea sandstone, along with the linear fit to the low pressure data. *Proprietary values are omitted from the axes labels.*

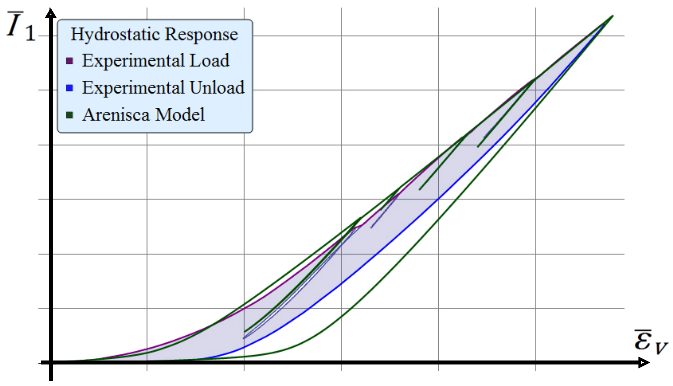

Figure 10: Experimental data for the hydrostatic load-unload response of drained Berea sandstone, and the simulated response obtained by fitting the empirical models for the bulk modulus and crush curve. *Proprietary values are omitted from the axes labels.*

slowly enough to avoid local plastic deformation, but does increase the pore pressure from the initial prescribed value. At the time of impact, the resulting "true initial pore pressure" will lie between the prescribed initial value and the confining stress.

Various combinations of constitutive model features are explored in Section 3.

2.3.2. Penetrator Description

The new methods described in this paper were developed to model the penetration of a shaped-charge jet into a porous rock target. As shown in Fig. 11, it is possible to model the formation of the shaped-charge jet using the MPM, but to more efficiently investigate the interactions between the penetrator and target, several types of imported penetrators were defined.

Using proprietary data from flash x-ray and time-of-arrival tests for a typical shaped charge (similar to the method described by Huang (2013)), a jet description was created that defines the mass, momentum and kinetic energy of the jet at a particular snapshot in time. The actual jet comprises a high velocity cloud of particulates that are much finer than the res-

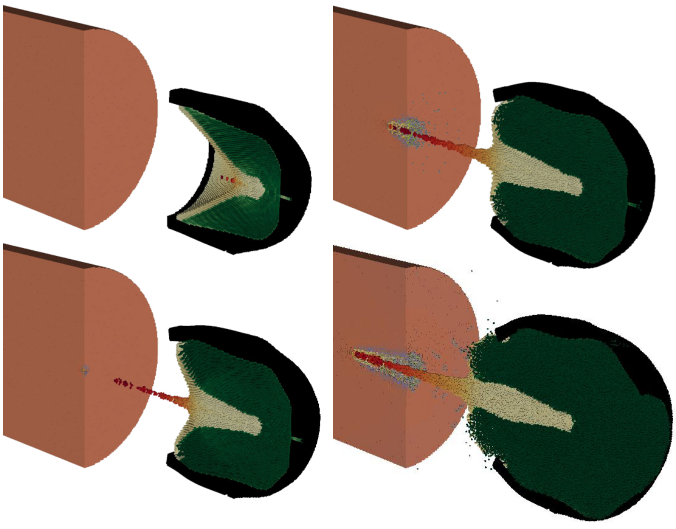

Figure 11: 3-D Uintah MPM simulation of shaped-charge jet formation and penetration into a sandstone target

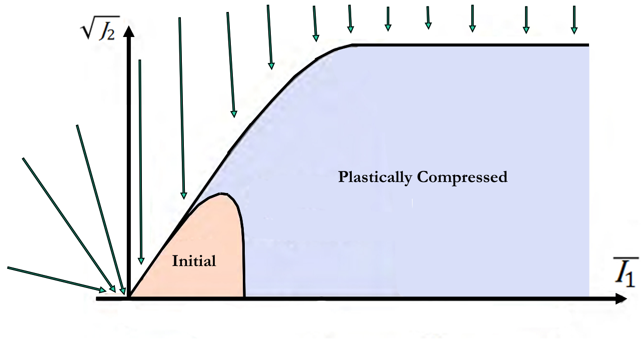

Figure 12: Illustration of the yield surface for the CVD jet. Arrows illustrate the nonassociative return directions from various trial state.

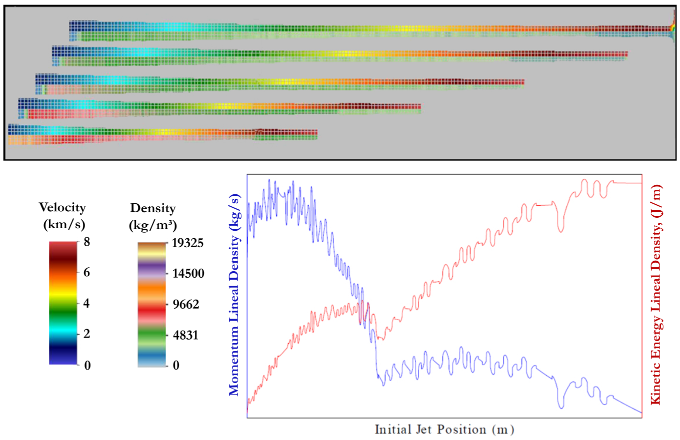

Figure 13: Expansion and impact of the continuous, variable-density jet showing contours of velocity and density (top), momentum and kinetic energy lineal densities in the initial jet description (inset). *Proprietary values are omitted from the axes labels.*

olution of the penetration simulations. Both the density and velocity are spatially varying, and the jet expands over time. Three approaches were taken to approximate this behavior.

The simplest approach defines a uniform tungsten rod with a total mass and kinetic energy matched to the measured properties of the jet. The length of the rod was defined so that the time over which 90% of the momentum flux occurred is the same as in the actual jet. This approach ignores the complexity of the jet, and also results in a very small penetrator diameter, which likely increases the simulation resolution needed to capture the correct constitutive response near the penetration channel.

The second approach defines a discrete jet of tungsten cylinders, each having a length, radius, and velocity specified to match the measured jet description (Burghardt et al., 2010). This approach is more reasonable, but produces a pulsed impact at the target, the frequency of which is dependent on discretization. Additionally, there is some evidence that the discrete jet increases the likelihood of kinematics errors that sometimes occur in MPM simulations, possibly due to numerical error associated with small-mass nodes in the numerical solution (Austin, 2013)

Finally, a continuum jet was defined with a continuous variable density (CVD) using the Arenisca constitutive model with parameters selected to achieve the desired response. The continuum jet has a spatially varying velocity, density, and radius. For each particle in the jet, the initial porosity is defined based on the density of the compacted jet material and the desired initial void fraction at the point. The crush curve is parameterized so that the initial hydrostatic compressive strength is quite small, and quickly evolves to a high value only when the initial void fraction has been compressed out. The shear limit surface is defined with a vertex at the origin, and a pressure response that quickly transitions to a von Mises surface at high pressure. Furthermore a nonassociative plastic flow is defined to ensure that the stress state remains at the vertex during dilatation. This is illustrated in Fig. 12. With this definition, the jet material will yield at near-zero stress during the initial free flight expansion, but as it impacts the target, the porosity is eliminated and the material response quickly becomes that of dense tungsten. Figure 13 shows free flight expansion and initial impact of the continuum jet, along with a profile of the momentum and kinetic energy density in the initial configuration. The apparent noise in the velocity profile results from the interpretation of the experimental data, which has been retained to mimic the fluctuations that would exist in a real jet.

3. Results

3.1. Hydrostatic Response

The implementation of the continuum effective-stress model is illustrated through a single- element prescribed-deformation test of the load-unload response. Fig. 14 shows the porosity vs. pressure for a drained and undrained material. To aid in interpreting these figures, each deformation path is also illustrated as a pressure vs. volumetric strain path. The drained material is loaded elastically from (A) to the initial yield at (B). Pores collapse from (B) to (C), at which point the strain is reversed so the material is unloaded until yielding in tension at (D). The tensile yield occurs at a constant stress from (D) to (E). The

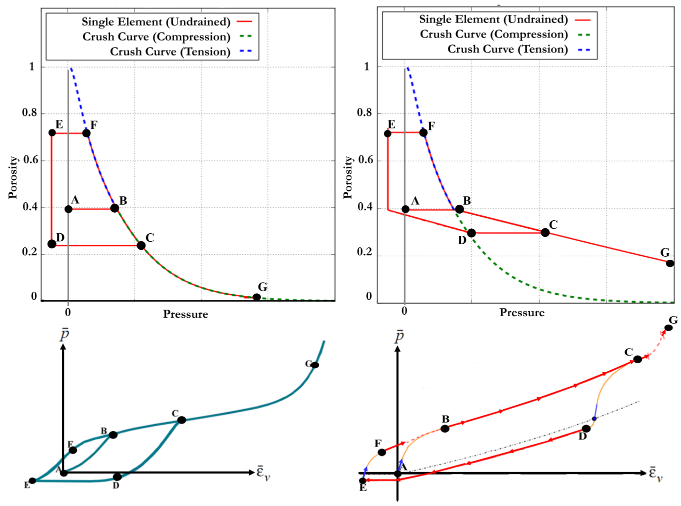

Figure 14: Single-element hydrostatic load-unload response of a drained (left) and undrained (right) material. The $\bar{p}$ vs. ε_v plots notionally illustrate the load paths, but are not actual results since it is difficult to see the elastic region in a plot of the true response over a scale sufficient to collapse pores.

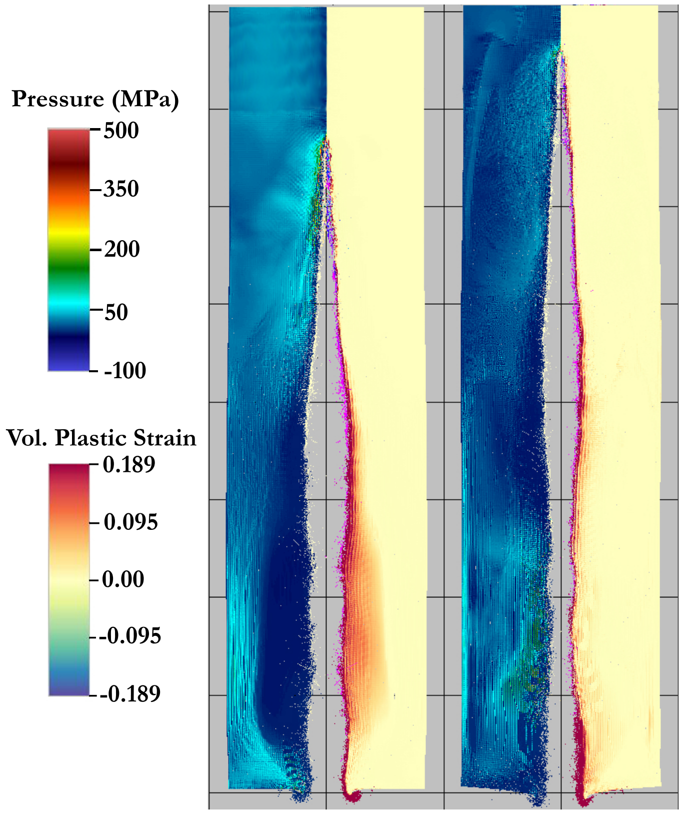

Figure 15: Penetration of a CVD jet into sandstone. Left: drained, $\bar{\sigma}^{m} = 25$MPa. Right: Undrained, $\bar{\sigma}^{m} = 10$MPa, $\bar{p}^{i}_{f} = 5$MPa Contours show pressure (left) and volumetric plastic strain (right) for the target along with velocity (left) and density (right) for the jet.

material is then recompressed to yield at (F), with continuing pore collapse from (F) to (G). The undrained material follows a similar deformation path. The response shows that the fluid slightly increases the initial hydrostatic compressive strength. The compressive response is noticeably shifted by the evolving isotropic backstress, but in spherical tension the response is equivalent to that of the drained material.

3.2. Penetration Simulations

The validity of the effective-stress approach described herein has been demonstrated though its application to the simulation of shaped-charge jet penetration into sandstone, with particular emphasis on the effects of initial pore pressure and confining stress on the final penetration channel and damaged region.

Figure 15 compares the penetration channel for a CVD jet shot into a preconfined drained sandstone target to that formed in a less confined undrained target with initial pore pressure. The results correctly show that the depth of penetration (DOP) is deeper for the undrained target, despite the increased target density. The drained and undrained responses are similar for the initial high-velocity phase when hydrodynamic effects dominate, but then the tail of the jet produces a very different response since constitutive effects dominate at lower jet velocities. One of the uncertainties in parametrization of the model is how to best define the shear modulus. For an isotropic elastic tangent stiffness to be thermodynamically consistent, the bulk modulus can depend on stress only through pressure, (if the elastic shear strains are nonnegligible) the shear modulus must be constant (Fuller and Brannon, 2013). However, measurements of the Poisson's ratio for Berea sandstone (inferred from measurements of Young's modulus) at different pressures (Hart and Wang, 1995) show a strong pressure dependence, likely a result of induced anisotropy. To identify the best choices for defining elastic properties within the confines of an isotropic tangent stiffness, we compute the bulk modulus in compression using the empirical hydrostatic model described previously, and then compute the shear modulus from that value and a pressure-dependent Poisson's ratio. The Poisson's ratio is defined as

$$\nu = g_1 + g_2 e^{-b_2/\bar{I}_1}, \tag{27}$$

where g_1 is the initial value, $g_1 + g_2$ is the high-pressure limit, and b_2 is the same shape parameter used for the pressure-dependent bulk modulus (Eq. 21). The effect of the Poisson's ratio scaling is shown in Fig. 16 for a broad range of Poisson's ratio values. The results show that pressure dependence of the shear modulus significantly affects both the channel geometry and depth of penetration. When the Poisson's ratio is allowed to increase significantly with pressure, this reflects the damage (decrease in shear modulus) that occurs with pore collapse. Much like nonassociativity, this becomes a tuning parameter that can be adjusted to fit experiments, but which should not be expected to provide predictive results when applied to simulations where the modes of deformation differ from those for which the model was tuned.

3.2.1. Simpler models

The results in Fig. 15 were obtained using an advanced CVD description of the jet, as well as nonlinear models for the strength and pressure-dependent elastic properties fit to the best

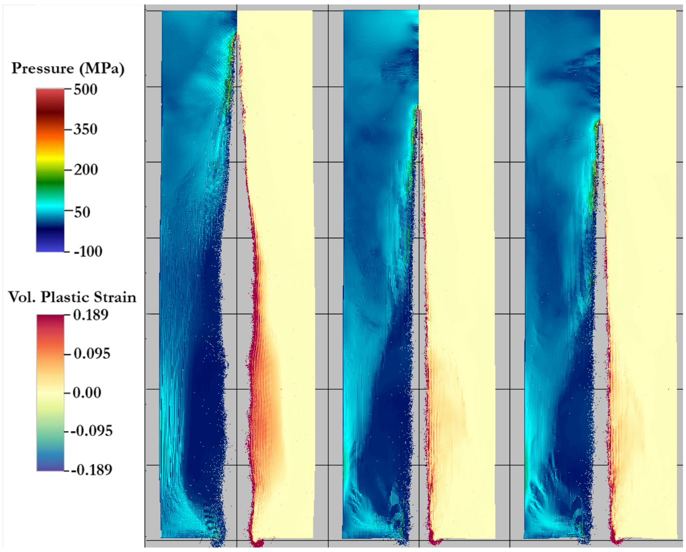

Figure 16: Comparison of penetration of a CVD jet into drained sandstone with 25MPa confining stress for various values of the Poisson's ratio scaling parameter g_2. Poisson's ratio increases with pressure (left), remains constant (center), and decreases (right).

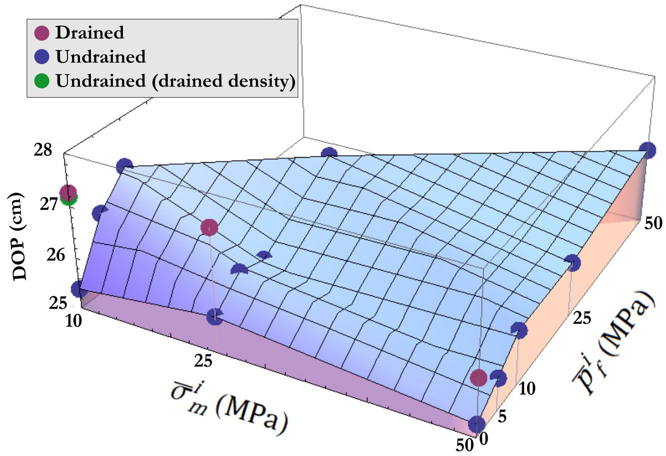

Figure 17: Trends in depth of penetration vs. pore pressure and confining stress for a tungsten rod into sandstone.

available data. The simulation response with simpler models was also investigated to determine the extent to which the correct trends could be obtained with a less detailed description of the target material. This section provides evidence that simpler models are generally inadequate.

The simplified simulations use a thin tungsten rod penetrator, and the target has a linear Drucker-Prager strength model (which over predicts the strength at high pressures as shown in Fig. 9), and a constant shear modulus (which overpredicts the Poisson's ratio at high pressure). Figure 17 shows the trends for thin rod penetration into drained and undrained sandstone with a range of initial pore pressures and confining stresses. Figure 18 shows the penetration channel formed for a subset of these simulations, all with 50MPa confining stress. The results in Fig. 17 show the correct general trend that confining stress decreases DOP while pore pressure increases DOP, but the drained data show a significantly deeper DOP than the corresponding undrained points. This suggests that while the constitutive model produces the correct trends, the trends are "weak" in the sense that the fluid-induced strength reduction is insufficient to compensate for the increased target density. To support this assertion, an additional simulation using the undrained constitutive model, but with density of the drained material, showed an increase in DOP approximately equal to the discrepancy between the drained and undrained tests.

Considering these results and those obtained with the CVD jet and more advanced target model, it is clear that while the effective-stress model can be implemented in a simplified framework, the resulting errors may overwhelm the effects of pore pressure in the simulation.

3.2.2. The Penetration Channel

The geometry of the penetration channel is used to compare the effect of constitutive model features and penetrator types.

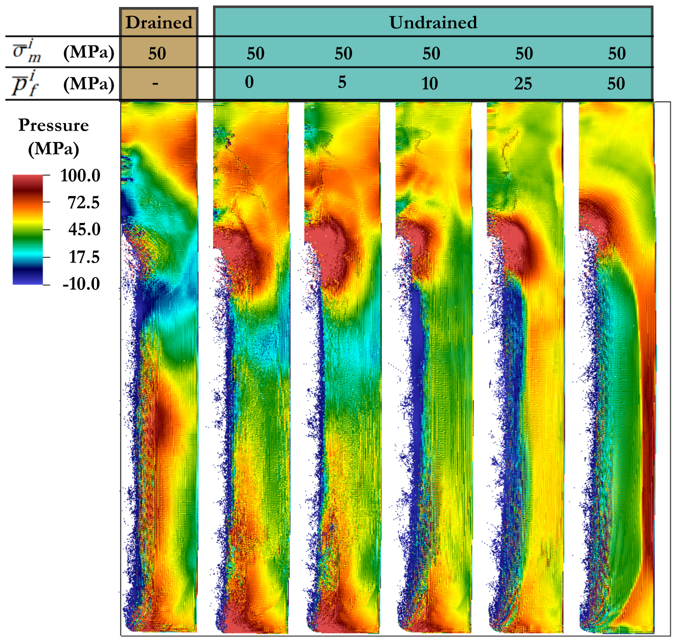

Figure 18: Penetration channel showing contours of pressure for a tungsten rod into a simplified model of drained and undrained sandstone. Each simulation has a 50MPa confining stress and a range of initial pore pressures.

MPM simulations do not explicitly track material surfaces, and while this allows for very efficient treatment of impact simulations with severe distortion, it also introduces uncertainty in defining the channel geometry.

Two approaches are taken to define the depth of penetration. Fig. 19 shows the penetrator slug in the channel tip, for which the DOP is determined from the deepest penetrating jet particle. While the variation in slug geometry introduces some error in the measurement, it does not appear sufficient to account for the non-monotonicity observed in Fig. 17.

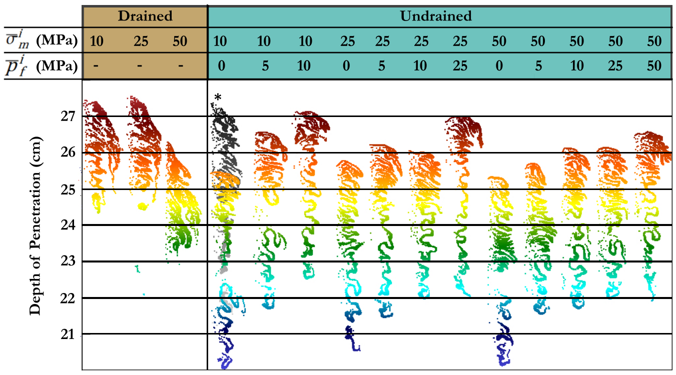

Figure 19: Jet material in the penetration channel tip for a tungsten rod penetrator into simplified drained and undrained sandstone, corresponding to the results in Fig. 17. The target density for the undrained material has been increased to account for the pore fluid, except for the (*) simulation in gray, which used a drained target density to quantify this effect.

In penetration experiments, the depth of penetration is typically measured for a cleaned channel, which has been scrubbed to remove loose debris. By defining a threshold of plastic deformation, we can visualize the region surrounding the channel that would likely be rubblized. An example of this alternative interpretation of DOP is shown in Fig. 20, which compares the volumetric plastic strain surrounding the penetration channel for a drained and undrained target. While the depth of penetration based on the jet material is similar for the two cases, there is a significant difference in the damaged region around the channel. The increased dilatation in the undrained target results from (i) reduced compressibility, which requires greater radial displacement to allow for the penetrator, and (ii) the plastic expansion during unloading resulting from the accumulated pore pressure.

3.2.3. Penetrator Type

A key value of the tools presented in this paper is the ability to evaluate the design of penetrator types and to tailor the design and selection of shaped charges to specific target materials. While we have thus far focused primarily on the target model, it is important to understand how the character of the penetration channel is affected by both the type of penetrator and the method by which the penetrator is approximated in the simulation.

The simulation results in Figs. 15 through 20 show that a very different response is obtained for the CVD jet compared to that of a thin tungsten rod having the same total mass and

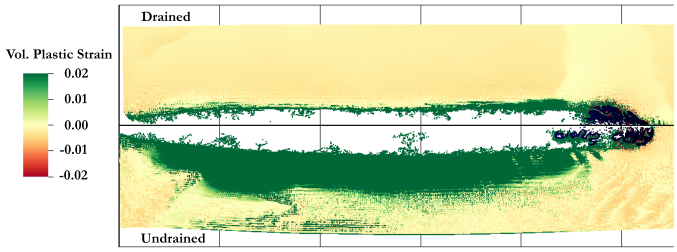

Figure 20: Penetration channel showing contours of volumetric plastic strain for a thin tungsten rod into a drained sandstone target with $\bar{\sigma}^m = 50MPa$ (top) and undrained an undrained sandstone with $\bar{\sigma}^m$ = 10MPa, $\bar{p}^i_f$ = 5MPa (bottom).

kinetic energy. A discrete jet was also investigated, which has nominally the same mass and velocity distribution as the CVD jet.

The discrete jet is desirable because it employs a simpler (and more efficient) constitutive model for dense tungsten, but the discretization of the jet is somewhat arbitrary, and it results in a pulsed momentum deposition that is not physically based, introducing uncertainty in the validity of the approach. Figure 21 compares the penetration of discrete and continuum jets into drained unconfined sandstone. While the results are similar, the discrete jet produces less depth of penetration relative to the continuous description. This difference could be due to smooth vs. pulsed momentum deposition, or due to the differences in contact area between the jet and target. While there is some minimal dissipation due to the plasticity approach used to allow expansion of the continuum jet, this would likely produce a decreased depth of penetration if it were a significant source of error.

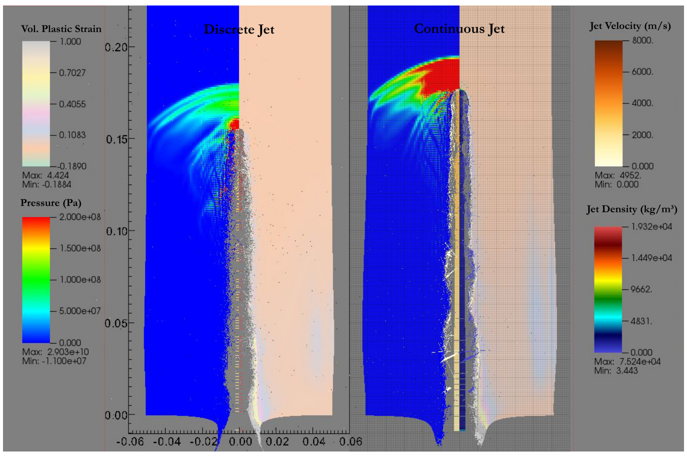

Figure 21: Penetration channel formation into an undrained target with no confining stress for a discrete jet (left) and continuum jet (right). Though the momentum and kinetic energy are matched for both jets, the continuum jet produces a deeper penetration channel.

3.2.4. Mesh Resolution

The results above have shown that the trends expected from the constitutive model manifest only weakly for the rod penetration simulations. This may be partially attributed to the small radius of the rod penetrator (1.5mm) relative to that of the discrete or continuous jet. Since the mesh resolution for the rod (Fig. 18) and jet (Fig. 21) tests were the same (1mm grid, 4 particles per cell (ppc)), the number of grid cells resolving the impact region was lower for the rod penetration.

To investigate mesh resolution effects, we compare the drained and undrained response for penetration of a shorter, 2mm radius rod (with the same mass and kinetic energy as the long-rod penetrator) and a higher mesh resolution (0.5mm grid, 4 ppc). For this simulation, the densities of both targets are the same to isolate the constitutive effects. The results in Fig. 22 show a much more significant increase in depth of penetration for the undrained target than was observed for the lower-resolution thin-rod penetrator tests, which supports the conjecture that the weak and nonmonotonic trends in Fig. 17 are at least partially attributable to under-resolution.

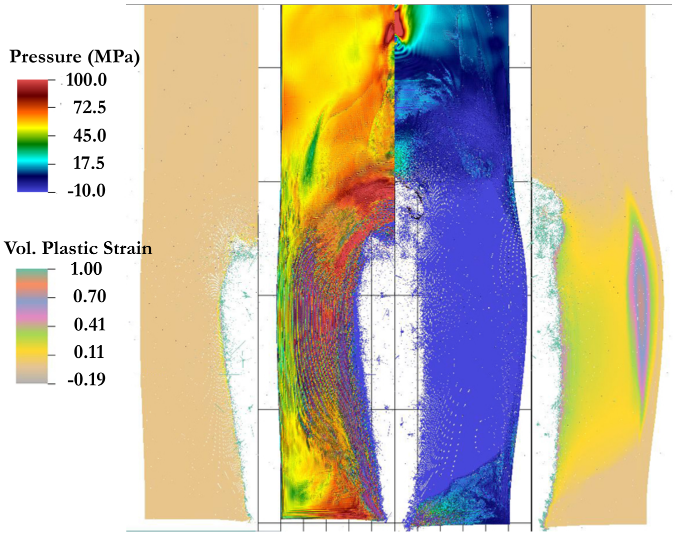

Figure 22: Penetration channel showing contours of pressure and volumetric plastic strain for a short rod penetrator into drained sandstone with $\bar{\sigma}^{m}$ = 50MPa (left) and undrained sandstone with $\bar{\sigma}^{m}$ = 10MPa $\bar{p}^{i}_{f}$ = 5MPa (right). The mesh resolution is 0.5mm.

The results in Fig. 15 show the correct trends using a 1mm mesh, with a particle density of 4 ppc for the jet and target core. To demonstrate convergence of the results, the same simulation is run using a resolution of 2mm and 0.5mm, as shown in Fig. 23. The convergence study shows that the depth of penetration increases and the channel narrows with refinement. The results suggest a weak convergence in that the change from the coarsest to the middle resolution is greater than that from the middle to fine resolution, but the coarsest simulation is severely under-resolved and has a very different channel structure from the other two. The differences between the drained and undrained simulations are more pronounced with higher resolution. Dependence of the results on mesh resolution is expected in problems with large shear deformation, in particular when the response is governed by the formation of shear bands. Shear band thickness will generally decrease with mesh refinement, unless a nonlocal constitutive model is used (Burghardt et al., 2012). The severe deformations at the channel surface

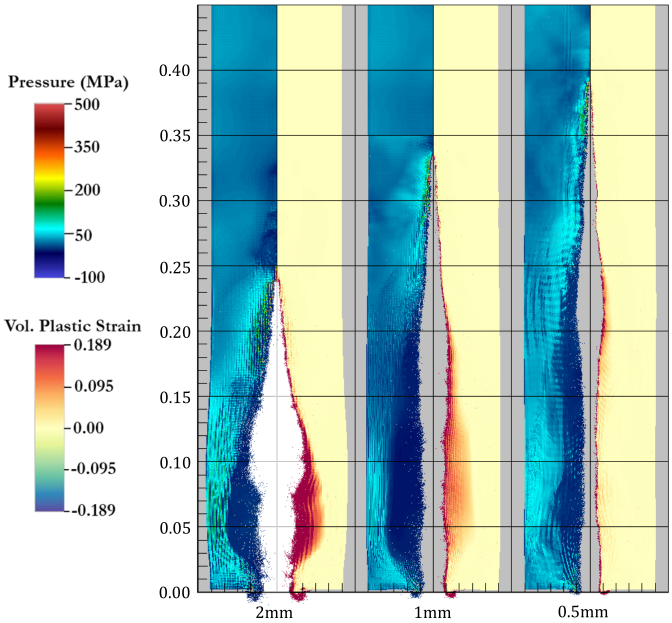

Figure 23: Mesh resolution dependence of penetration channel for CVD jet into drained sandstone. Grid resolution increases 2mm,1mm,0.5mm, from left to right.

make it difficult to detect specific shear bands, but there is a clear decrease in the thickness of the damaged region at higher resolution. Nonlocal models can introduce significant cost and complication to the solution method, particularly in parallelized codes. However, the undesirable mesh dependence can be mitigated somewhat by introducing statistical variability and concomitant scale effects in the material strength. This introduces a distribution of weak points to initialize failure, that are spatially distributed with a length scale independent of the mesh resolution (Strack et al., 2014).

3.2.5. *Visualization of Stress States During Penetration*

To better understand the role of the constitutive model, a new approach was used to visualize the stress state in the target material throughout the penetration event. While it is common to visualize simulations by plotting contours of the pressure or the magnitude of the shear stress, this does not allow direct comparison of results to plots of the yield surface for full-stress constitutive models.

To allow this comparison, two scalar field plots were generated over the problem domain, one of equivalent shear stress and one of pressure. The color maps are black to yellow, and cyan to magenta, respectively so that a 50 percent opacity overlay of the two images creates a CMYK colormap of the stress state.

The stress state during penetration is shown in Fig. 24, for a tungsten rod shot into a drained sandstone target. The stress state extends well beyond the initial yield surface. In the compressive region, this is partially attributed to hardening (expansion of the porosity cap), but low-pressure, high-shear stresses also arise that lie outside the shear limit surface. This is attributed to the viscoplastic overstress that occurs at high loading

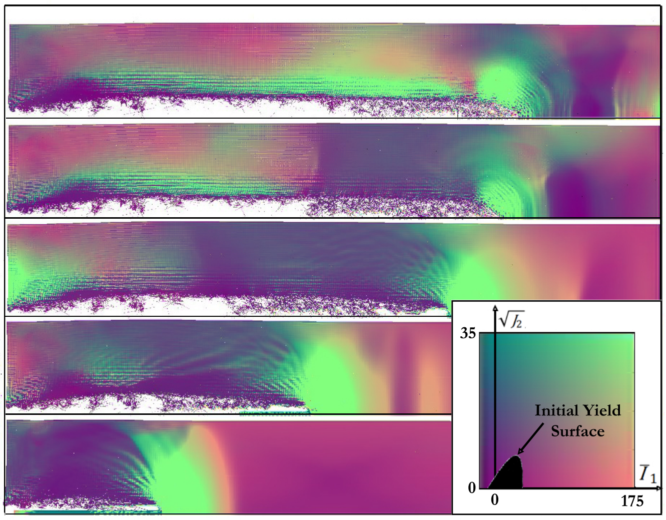

Figure 24: Penetration of a tungsten rod into drained sandstone with 25 MPa confining stress. Contours map to stress space legend (inlaid) shown along with the meridional profile of the initial yield surface.

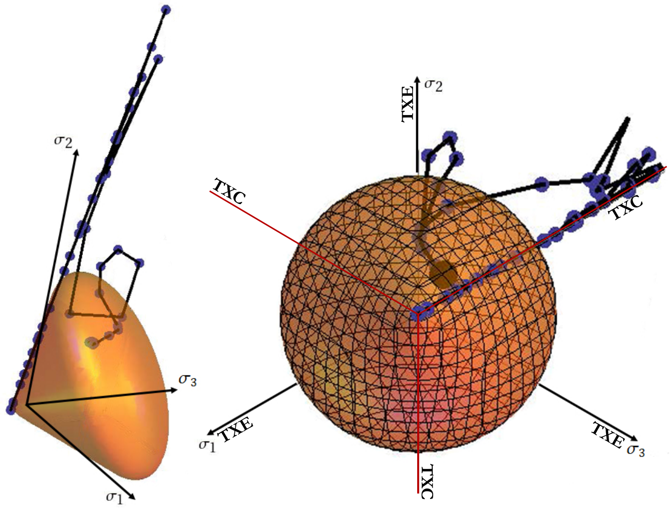

Figure 25: Path through 3D principal stress space (left) and the octahedral plane (right) of a particle of target material near the penetration channel, shown with a rendering of the Arenisca yield surface

rates.

3.2.6. Third invariant dependence

In the previous simulations, the target yield surface is defined in the meridional plane of stress space by yield criteria that depend only on pressure and shear stress. This neglects the variation in strength between triaxial compression (TXC) and triaxial extension (TXE), (*i.e.,* "Lode angle" or "third-invariant" dependence), which is known to be significant for geomaterials (Pivonka and Willam, 2003; Schreyer and Bean, 1985).

The stress path for a particle near the penetrator tip was rendered in order to illustrate the Lode angle of the stresses within the target material. Fig. 25 shows the stress path relative to the initial yield surface in 3D principal stress space and in the octahedral profile. Since the ordering of the principal stresses is arbitrary, the path is confined to a sextant of the octahedral profile. There is significant Lode angle variation throughout the load history within that sextant, which suggests that the ability to simulate 3$^{\text{rd}}$-invariant dependence may be important in obtaining predictive results. To investigate the effect of Lode-angle dependence, a penetration simulation was run using a Mohr-Coulomb type 3$^{\text{rd}}$invariant dependence, with ratio of TXC/TXE strength of 1.2. Figure 26 compares the results of a CVD jet penetration into drained sandstone with and without the 3$^{\text{rd}}$invariant dependence. The results show that there is a wide range of Lode angle states throughout the target. While there are some subtle differences in the stress state and channel geometry, the results show there is not a significant effect on the channel geometry or depth of penetration, suggesting that Lode angle dependence plays only a minor role in penetration response.

4. Discussion and Conclusions

The results of numerical simulations suggest that an effective stress model, when implemented as an isotropic backstress, is sufficient to capture the key features in the response of penetration to pore fluid and confining stress, but only when the constitutive model is of sufficient fidelity to describe the response of the material.

In developing the methods described herein, a key constraint was the need to parameterize the model from a limited set of tractable experimental methods. This makes it practical to apply the model for a wide variety of target materials.

4.1. Limitations

The constitutive model is only as accurate as the data from which it is parametrized. Significant experimental error may exist, and in some cases the stresses in penetration simulations may lie well outside the range of experiments used to characterize the material. However, even where empirical models are used, we have endeavored to develop functional forms that produce the reasonable trends in limiting cases, improving the predictions when extrapolation is needed.

The isotropic constitutive model does not account for the initial anisotropy from the bedding planes of the sedimentary rock, nor the induced anisotropy that no doubt occurs during deformation. Induced anisotropy is an important phenomenon, and has been postulated to be the true mechanism behind the experimental response that has motivated nonassociative plasticity as well as pressure dependence of the shear modulus (Fuller and Brannon, 2013).

As formulated, this approach is limited to applications where the fluid pressure can be determined from material properties, initial conditions, and the local deformation state. This implies that either the porosity must be disconnected or the loading rates must be sufficiently high that fluid transport through the

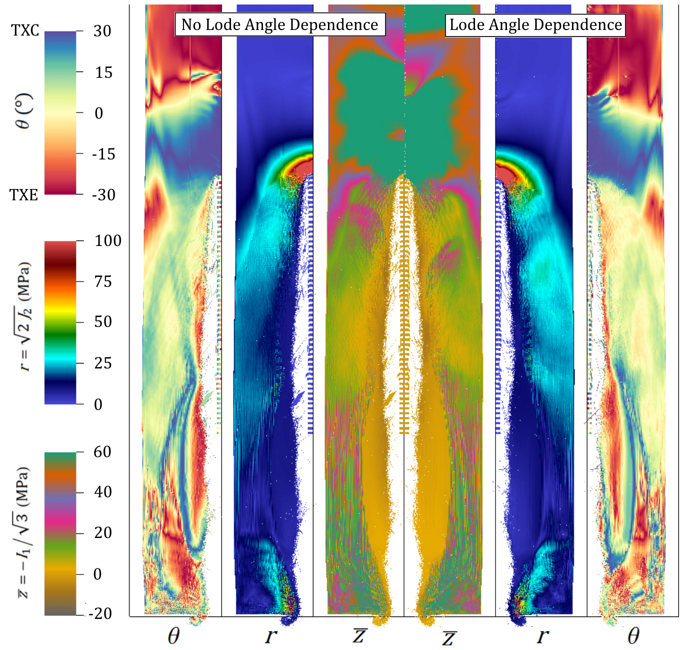

Figure 26: Comparison of of the target stress state during penetration at 170 µs. The target is drained sandstone with 25 MPa confining stress. The target on the left has no Lode angle dependence. The target on the right is identical but with a Mohr-Coulomb strength model and a TXC to TXE strength ratio of 1.2.

matrix can be neglected. Extending the approach to lower loading rates requires solving for multiple velocity fields and allowing the fluid mass flux into the material to modify the effective value of $\bar{p}^i_f$. Additionally it would be necessary to define a relationship between plastic deformation, damage, and permeability.

The work has assumed high rates, which would normally be associated with adiabatic deformation, but the effect of temperature on the constitutive response (*e.g.,* differences in isothermal and isentropic moduli) has been neglected. The added expense of including thermal effects in the constitutive model would not clearly be justified by the added value in application to comparative shaped charge jet design.

The approach has been presented using a very simple fluid equation of state, which only roughly approximates the isothermal compressibility of liquid water. Furthermore, the use of isothermal (rather than adiabatic) equation-of-state data is questionable for high-rate loading, but this was done in order to be consistent with the compressibility of the grains, which is inferred from measurements of the high-pressure response in quasistatic hydrostatic compression. This was done to preserve the porosity-volume relationship, which depends on the relative compressibility of the fluid and grain. To some extent, the difference between this approach and the true response is compensated for in the empirical model of rate dependence.

Previous work has shown that a time-to-failure damage model, along with perturbation of initial strength by statistical variability and scale effects helps to mitigate mesh dependence, allowing for more realistic brittle failure (Strack et al., 2014). For this effort, the constitutive response has neglected softening except through cap retraction in dilatation, and does not model damage except through the elastic-plastic coupling effect in the bulk modulus. While there is certainly significant degradation of the material strength in the heavily deformed region, the application of a softening model within an axisymmetric simulation is questionable, since radial cracking cannot occur. As a result, nonphysical radial expansion is observed for simulations with low confining pressure, (*c.f.,* Fig. 22). Using the methods described herein in a full 3-D simulation that included a realistic brittle failure model would likely result in improved predictions of the damaged region around the channel, especially at lower pressures, but would significantly increase the computational expense. The addition of a damage model has been shown by Vorobiev et al. (2007) to be significant factor in penetration simulations of metal projectiles, and would likely also be play a significant role with shaped-charge jet penetration.

Finally, the internal state variable evolution laws given in Eq. 9 and Eq. 26 are suitable for implementation into a conventional plasticity framework (*c.f.,* Brannon (2007)). However, these evolution laws are highly nonlinear, and care must be taken in the numerical solution to obtain a stable and accurate result. Details of our implementation for numerical solution are given in Homel and Brannon (2014), which describes these issues as well as several other challenges specific to this class of model.

4.2. Capabilities

To our knowledge, the effective stress model described herein is the only such tool capable of simulating the effects of an evolving pore pressure in both elastic and plastic deformation, while allowing for specification of an initial pore pressure and confining stress, and maintaining the necessary capabilities of a geomechanics constitutive model.

This capability has allowed for predictive quality in penetration simulations that was previously unobtainable.

While the empirical models for the various features (bulk modulus, crush curve, limit surface, rate dependence, etc.) in the models were fit to the best data from standard calibration tests (*e.g.,* hydrostatic compression, triaxial compression, etc.), there was no parameter tuning to achieve the desired response from the penetration simulation. That the results predicted both the correct trends, and reasonable quantitative values is a key step in validating the assumptions made in formulating the model.

4.3. Conclusions

A continuum constitutive modeling approach has been developed to implement the effective stress concept with a pore pressure that evolves with plastic deformation. This is a powerful tool that may be helpful in the design of shaped-charge jet technologies and other applications that involve high-rate deformation of fluid-saturated porous materials.

The model development is motivated by an analytical model of a saturated thick spherical shell, which led to an isotropic backstress as an additional state variable in a full-featured plasticity model for geomaterials. In combination with poroelasticity theory and a strain-to-yield approach, the response of the drained material can be predicted using parameters obtained from tractable experiments on the drained material.

A continuum description of the shaped charge jet allows for an initial void fraction to closely match the density, velocity and geometry profile measured from a real jet. This approach was shown to produce much more realistic trends than either a solid or discrete jet description.

This work has surveyed the influence of a variety of physical phenomena and model features, to determine the effect each has on the penetration response. The results indicate that the correct trends in depth of penetration vs. pore pressure can be achieved with the effective stress model in combination with the CVD jet, but these trends are not strongly evident when simpler models for the penetrator or target are used.

Application of the model is made tractable through several simplifying assumptions, but even with these limitations it appears well-suited for comparative analysis of various target/jet combinations.

Acknowledgements. Primary support of this work by Schlumberger Technology Corporation is gratefully acknowledged. Valuable assistance in developing the Arenisca constitutive model was provided by James W. Colovos. Interactions with other University of Utah researchers under ONR MURI grant N00014-11-1-0691 is also acknowledged. Essential computational resources provided by the University of Utah center for high performance computing.

5. References

1. Karrech, A., Poulet, T., Regenauer-Lieb, K.. Poromechanics of saturated media based on the logarithmic finite strain. *Mechanics of Materials* 2012; **51**:118–136.
2. Wang, H.F.. *Theory of Linear Poroelasticity with Applications to Geomechanics and Hydrogeology*. Princeton Press; 2000.
3. Swan, C., Lakes, R., Brand, R., Stewart, K.. Micromechanically based poroelastic modeling of fluid flow in haversian bone. *Transactions-ASME J Biomechanical Engineering* 2003;**125**(1):25–37.
4. Kohles, S.S., Roberts, J.B., et al. Linear poroelastic cancellous bone anisotropy: trabecular solid elastic and fluid transport properties. *Transactions-ASME J Biomechanical Engineering* 2002;**124**(5):521–526.
5. Borja, R.I.. On the mechanical energy and effective stress in saturated and unsaturated porous continua. *International journal of solids and structures* 2006;**43**(6):1764–1786.
6. Gupta, A., Bayraktar, H.H., Fox, J.C., Keaveny, T.M., Papadopoulos, P.. Constitutive modeling and algorithmic implementation of a plasticity-like model for trabecular bone structures. *Computational Mechanics* 2007; **40**(1):61–72.
7. Scambos, T.A., Hulbe, C., Fahnestock, M., Bohlander, J.. The link between climate warming and break-up of ice shelves in the antarctic peninsula. *Journal of Glaciology* 2000;**46**(154):516–530.
8. Kamb, B.. Rheological nonlinearity and flow instability in the deforming bed mechanism of ice stream motion. *Journal of Geophysical Research: Solid Earth (1978–2012)* 1991;**96**(B10):16585–16595.
9. Strack, O.E., Leavy, R.B., Brannon, R.M.. Aleatory uncertainty and scale effects in computational damage models for failure and fragmentation. *Int J Numerical Methods in Engr* 2014;**Special Issue celebrating the 70th birthday of Ted Belytschko**:In Press.
10. Geiser;, N.K.F., Blight, G.. Effective stress in unsaturated soils: Review with new evidence. *Int J of Geomechanics* 2004;**4**(2):115–126.
11. Terzaghi, K.. The shearing resistance of saturated soils and the angle between planes of shear. *First Int Conf on Soil Mech and Found Engr,Harvard University* 1936;**I**:54–56.
12. Fillunger, P.. Versuche uber die zugfestigkeit bei allseitigem wasserduck. *OesterrWochenschrift oeffent Baudienst* 1915;**29**:443–448.
13. Schrefler, B.A., Gawin, D.Z.. The effective stress principle: Incremental or finite form? *Int J for Numerical and Analytical Methods in Geomechanics* 1996;**20**(11):785–814.
14. Biot, M.A.. Theory of propagation of elastic waves in a fluid-saturated porous solid. i. low-frequency range. *The Journal of the Acoustical Society of America* 1956;**28**:168.
15. Biot, M.A.. General theory of three-dimensional consolidation. *Journal of applied physics* 1941;**12**(2):155–164.
16. Nedjar, B.. Formulation of a nonlinear porosity law for fully saturated porous media at finite strains. *Journal of the Mechanics and Physics of Solids* 2012; .
17. Nur, A., Byerlee, J.. An exact effective stress law for elastic deformation of rock with fluids. *J of Geophysics Research* 1971;**76**(26):6414–6419.
18. Sun, D., Sheng, D., Sloan, S.W.. Elastoplastic modelling of hydraulic and stress–strain behaviour of unsaturated soils. *Mechanics of Materials* 2007; **39**(3):212–221.
19. Anandarajah, A.. *Computational Methods in Elasticity and Plasticity: Solids and Porous Media*. Springer; 2010. ISBN 9781441963789.
20. Scholts, L., Hicher, P.Y., Nicot, F., Chareyre, B., Darve, F.. On the capillary stress tensor in wet granular materials. *International Journal for Numerical and Analytical Methods in Geomechanics* 2009;**33**(10):1289–1313. doi:10.1002/nag.767.
21. Xie, S., Shao, J.. Experimental investigation and poroplastic modelling of saturated porous geomaterials. *International Journal of Plasticity* 2012; **39**(0):27–45. doi:10.1016/j.ijplas.2012.05.007.
22. Sheng, D., Zhang, S., Yu, Z.. Unanswered questions in unsaturated soil mechanics. *Science China Technological Sciences* 2013;:1–16.
23. Nedjar, B.. Poromechanics approach for modeling closed-cell porous materials with soft matrices. *International Journal of Solids and Structures* 2013;.
24. Jaegar, J., Cook, N.. *Fundamentals of Rock Mechanics*. Chapman Hall; 1976.
25. Goodman, R.. *Introduction to Rock Mechanics*. John Wiley; 1980.
26. Buhan, P.D., Dormieux, L.. On the validity of the effective stress concept for assessing the strength of saturated porous materials: A homogenization approach. *J of the Mech and Physics of Solids* 1996;**44**(10):1649 – 1667.
27. Barthelemy, J., Dormieux, L.. On the existence of an effective stress in poroplasticity. In: *Poromechanics III-Biot Centennial (1905-2005): Proceedings of the 3rd Biot Conference on Poromechanics, 24-27 May 2005, Norman, Oklahoma, USA*; vol. 1000. Taylor & Francis; 2010, p. 129.
28. Coussy, O.. *Mechanics of Porous Continua*. John Wiley; 1995.
29. Lomov, I., Hiltl, M., Vorobiev, O.Y., Glenn, L.. Dynamic behavior of berea sandstone for dry and water-saturated conditions. *International journal of impact engineering* 2001;**26**(1):465–474.
30. Wilmanski, K.. A few remarks on biot's model and linear acoustics of poroelastic saturated materials. *Soil Dynamics and earthquake engineering* 2006; **26**(6):509–536.
31. Cooper, P.W.. Scaling and explosives engineering applications. *Sandia National Laboratories Short Course* 2007;**XPL204**.
32. Grove, B., Heiland, J., Walton, I.. Geologic materials' response to shaped charge penetration. *International Journal of Impact Engineering* 2008; **35**(12):1563 – 1566.
33. Lee, N.S., Bathe, K.J.. Error indicators and adaptive remeshing in large deformation finite element analysis. *Finite Elements in Analysis and Design* 1994;**16**(2):99 – 139. doi:http://dx.doi.org/10.1016/0168-874X(94)90044-2.
34. Antoun, T., Glenn, L., Walton, O., Goldstein, P., Lomov, I., Liu, B.. Simulation of hypervelocity penetration in limestone. *International journal of impact engineering* 2006;**33**(1):45–52.
35. Liu, W.K., Belytschko, T., Chang, H.. An arbitrary lagrangian-eulerian finite element method for path-dependent materials. *Computer Methods in Applied Mechanics and Engineering* 1986;**58**(2):227–245.
36. Bardenhagen, S., Brackbill, J., Sulsky, D.. The material-point method for granular materials. *Computer methods in applied mechanics and engineering* 2000;**187**(3):529–541.
37. Guilkey, J., Harman, T., Luitjens, J., Schmidt, J., Thornock, J., Davison de St. Germain, J., et al. Uintah user guide version 1.1. *SCI Institute, University of Utah* 2009;**UUSCI-2009-007**.
38. Carroll, M.M., Holt, A.C.. Static and dynamic pore collapse relations for ductile porous materials. *J of App Physics* 1972;**43**(4):1626 –1636.
39. de Borst, R., Pamin, J., Geers, M.G.. On coupled gradient-dependent plasticity and damage theories with a view to localization analysis. *European*

Journal of Mechanics-A/Solids 1999;**18**(6):939–962.
40. Morris, J., Lomov, I., Glenn, L.. A constitutive model for stress-induced permeability and porosity evolution of berea sandstone. *Journal of geophysical research* 2003;**108**(B10):2485.
41. Gassmann, F.. Elasticity of porous media. *Vierteljahrsschrder Naturforschenden Gesselschaft* 1951;**96**:1–23.
42. Hart, D.J., Wang, H.F.. Laboratory measurements of a complete set of poroelastic moduli for berea sandstone and indiana limestone. *Journal of Geophysical Research: Solid Earth (1978–2012)* 1995;**100**(B9):17741–17751.
43. Pietruszczak, S., Pande, G.. On the mechanical response of saturated cemented materialspart i: theoretical considerations. *International journal for numerical and analytical methods in geomechanics* 1995;**19**(8):555–562.
44. Brannon, R., Fossum, A., Strack, O.. Kayenta: Theory and user's guide. *Sandia Report* 2009;**2009**(2282):393–397.
45. Li, Y.H.. Equation of state of water and sea water. *J of Geophysical Research* 1967;**72**(10):2665–2678.
46. Homel, M., Guilkey, J., Brannon, R.. Mesoscale investigation of the effective stress approach in elastoplastic deformation of geologic materials using the material point method 2014a;.
47. Sulsky, D., Zhou, S., Schreyer, H.. Application of a particle-in-cell method to solid mechanics. *Computer Physics Communications* 1995;**87**:236–252.
48. Bardenhagen, S., Kober, E.. The generalized interpolation material point method. *Computer Modeling in Engineering and Sciences* 2004;**5**(6):477–496.
49. Austin, D.. *Verification and Validation of a Geomodel Aimed at Simulating Wellbore Completion via Shaped-Charge Jet Perforation of Metal and Penetration into Sandstone*. Master's thesis; University of Utah; 2013.
50. Homel, M., Sadeghirad, A., Austin, D., Colovos, J., Brannon, R., Guilkey, J.. Arenisca: Theory and users guide. Tech. Rep.; University of Utah; 2014b.
51. Bobich, J.K.. *Experimental analysis of the extension to shear fracture transition in Berea Sandstone*. Ph.D. thesis; Texas A&M University; 2005.
52. Burghardt, J., Brannon, R., Guilkey, J.. A nonlocal plasticity formulation for the material point method. *Computer Methods in Applied Mechanics and Engineering* 2012;**225**:55–64.
53. Simo, J., Hughes, T.. *Computational Inelasticity*. Interdisciplinary applied mathematics: Mechanics and materials. Springer; 1998. ISBN 9780387975207.
54. Huang, H.. Characterization of powder metal jet and penetration calculation. *Procedia Engineering* 2013;**58**:471–478.
55. Burghardt, J., Leavy, B., Guilkey, J., Xue, Z., Brannon, R.. Application of uintah-mpm to shaped charge jet penetration of aluminum. In: *9th World Congress on Computational Mechanics, IOP Conf. Series: Materials Science and Engineering, v.10.* 2010, .
56. Fuller, T., Brannon, R.. On the effects of deformation induced anisotropy in isotropic materials. *International Journal for Numerical and Analytical Methods in Geomechanics* 2013;**37**(9):1079–1094.
57. Pivonka, P., Willam, K.. The effect of the third invariant in computational plasticity. *Engineering Computations* 2003;**20**(5/6):741–753.
58. Schreyer, H.L., Bean, J.E.. Third-invariant model for rate-dependent soils. *Journal of Geotechnical Engineering* 1985;**111**(2):181–192.
59. Vorobiev, O.Y., Liu, B., Lomov, I., Antoun, T.. Simulation of penetration into porous geologic media. *International journal of impact engineering* 2007; **34**(4):721–731.
60. Brannon, R.M.. Elements of phenomenological plasticity. *Springer* 2007;.
61. Homel, M., Brannon, R.. Numerical solution for plasticity models using consistency bisection and a transformed-space closest-point return (cb-tscpr). *International Journal for Numerical Methods in Engineering* 2014;.

Appendix A. Derivation of the Spherical Shell Model

In this section the steady-state response is derived for an incompressible, linear-elastic, perfectly-plastic, thick spherical shell containing a pore fluid. The derivation is identical to that presented by Carroll and Holt (1972), except for the addition of a single term which accounts for the pore pressure at the inner surface. This confirms that an effective stress formulation is valid for the model. Additionally, the analysis has been extended into the tensile domain, which provides some insight into the nucleation of pores from small defects.

The spherical shell has inner radius, a and outer radius, b as depicted in Eq. 1. The shell is linear elastic with shear modulus G, and perfectly plastic with a yield stress Y. A pressure $\bar{p}_b$ acts on the outer surface of the material, and a pore pressure $(\bar{p}_a = \bar{p}_a)$ acts on the inner surface.

The solution is derived in terms of the distension (α), (the ratio of the total volume to the solid volume, $\alpha = V/V_s$, for $1 \leq \alpha$), but the results are presented in terms of the more intuitive variables for porosity and volumetric strain.

Appendix A.1. Spherical Equations of Motion

We begin with a general spherically symmetric motion, where the Eulerian and Lagrangian spherical coordinates are related by $r = r(r_0, t)$. For the motion to be isochoric, the Jacobian of the deformation must be 1 so:[2]

$$\frac{r^2}{r_0^2}\frac{\partial r}{\partial r_0} = 1 \tag{A.1}$$

Separating Eq. A.1 and integrating:

$$r^3 = r_0^3 - B(t) \tag{A.2}$$

Differentiating Eq. A.2 with respect to time:

$$3r^2 r' = -B(t) \tag{A.3}$$

Differentiating Eq. A.3 with respect to time

$$3r^2 r'' + 6r\,(r')^2 = -B''(t) \tag{A.4}$$

Using Eq. A.3 to eliminate r' from Eq. A.4

$$\frac{2B'(t)^2}{3r^3} + 3r^2 r'' = -B''(t) \tag{A.5}$$

Solving for d^2r/dt^2

$$r'' = \frac{-1}{9r^5}(3r^3 + B''(t) + 2B'(t)^2) \tag{A.6}$$

Defining an integration potential $\psi(r,t)$

$$\psi(r,t) = \int \frac{1}{9}\left(\frac{3B''(t)}{r} + \frac{B'(t)^2}{2r^4}\right) dr \tag{A.7}$$

[2] This equation was typeset incorrectly in the original Carroll and Holt (1972) publication.

We define an infinitesimal displacement

$$u(r,t) = -B(t)/3r^2, \tag{A.8}$$

and principal strains,

$$\epsilon_r(r,t) = 2B(t)/3r^3 \tag{A.9}$$

$$\epsilon_\theta(r,t) = \epsilon_\phi(r,t) = -B(t)/3r^3 \tag{A.10}$$

The principal deviatoric stresses are

$$s_r(r,t) = 2G\epsilon_r(r,t) \tag{A.11}$$

$$s_\theta(r,t) = s_\phi(r,t) = 2G\epsilon_\theta(r,t) \tag{A.12}$$

from which we define the principal stresses

$$\sigma_r = -p(r,t) + s_r(r,t) \tag{A.13}$$

$$\sigma_\theta = \sigma_\phi = -p(r,t) + s_\theta(r,t) \tag{A.14}$$

The radial equation of motion in terms of the integration potential is

$$\frac{\partial \sigma_r(r,t)}{\partial r} + \frac{2}{r}\left[\sigma_r(r,t) - \sigma_\theta(r,t)\right] = \rho \frac{\partial \psi(r,t)}{\partial r}. \tag{A.15}$$

Integrating this with respect to r to gives

$$-p(r,t) = -\frac{1}{9}\rho\left(-\frac{3B''(t)}{r} - \frac{B'(t)^2}{2r^4}\right), \tag{A.16}$$

where we can substitute the integration potential to obtain

$$-p(r,t) = \frac{\rho}{9}\left(\frac{3B''(t)}{r} + \frac{B'(t)^2}{2r^4}\right) + h(t), \tag{A.17}$$

where $h(t)$ is an integration constant.

Applying boundary conditions we can eliminate $p(r,t)$ at the boundary. At the inner surface ($r = a$), pressure is a function of the change in pore volume and the bulk modulus of the fluid (K_f).

$$\sigma_r^a = -\bar{p}_a \tag{A.18}$$

At the outer surface, the radial stress is the material pressure, which may vary with time:

$$\sigma_r^b = -\bar{p}_b \tag{A.19}$$

We can then define the internal pressure at the boundaries, for substitution into the integrated equation of motion:

$$p_a = s_r(a,t) - \sigma_r^a = \frac{4GB(t)}{3a^2} - \bar{p}_a \tag{A.20}$$

$$p_b = s_r(b,t) - \sigma_r^a = \frac{4GB(t)}{3b^3} + \bar{p}_b \tag{A.21}$$

We eliminate $h(t)$ by evaluating the integral over $a \le r \le b$

$$-p_b + p_a = \rho\left[\psi(b,t) - \psi(r,t)\right] \tag{A.22}$$

Expressing $B(t)$, $B'(t)$, and $B''(t)$ in terms of the distension (α), unloaded distension α_0, and unloaded pore radius (a_0) we get

$$B(t) = a_0^3 \frac{\alpha_0 - \alpha(t)}{\alpha_0 - 1} \tag{A.23}$$

$$B'(t) = -\frac{a_0^3 \alpha'(t)}{\alpha_0 - 1} \tag{A.24}$$

$$B''(t) = -\frac{a_0^3 \alpha''(t)}{\alpha_0 - 1}. \tag{A.25}$$

We then evaluate the integration potential at the boundary

$$\psi(a,t) = \frac{1}{9}\left(\frac{a_0^6 \alpha'(t)^2}{2a^4(\alpha_0 - 1)^2} - \frac{3a_0^3 \alpha''(t)}{a(\alpha_0 - 1)}\right) \tag{A.26}$$

$$\psi(b,t) = \frac{1}{9}\left(\frac{a_0^6 \alpha'(t)^2}{2b^4(\alpha_0 - 1)^2} - \frac{3a_0^3 \alpha''(t)}{b(\alpha_0 - 1)}\right) \tag{A.27}$$

The inner and outer shell radius can then be defined int terms of the distension, initial distention, and the initial inner radius:

$$a = a_0 \sqrt[3]{\frac{\alpha - 1}{\alpha_0 - 1}} \tag{A.28}$$

$$b = a_0 \sqrt[3]{\frac{\alpha}{\alpha_0 - 1}} \tag{A.29}$$

Appendix A.2. Solution

For the steady state solution, $\psi(a,t) = \psi(b,t) = 0$. Substituting Eq. A.20 and Eq. A.21 into Eq. A.22, and using Eq. A.28, Eq. A.29, and Eq. A.23 we obtain:

$$\overbrace{\bar{p}_b - \bar{p}_a}^{\text{EffectiveStress}} = \frac{4G(\alpha_0 - \alpha)}{3\alpha(\alpha - 1)} \tag{A.30}$$

The right hand side of this result is identical to the Carroll and Holt solution for the drained material, but has now been expressed in terms of an effective stress. The expression holds in both pore collapse and expansion.

The elastic limit is found by solving Eq. A.30 for the distension at which the inner surface is at the yield stress. Setting $(s_r(a) - s_\theta(a))$ equal to Y gives the limit distension (α_c^E) in pore collapse.

$$\alpha_c^{\mathbf{EP}} = \frac{2\alpha_0 G + Y}{2G + Y} \tag{A.31}$$

As the shell deforms, the stress increases until the inner surface reaches the yield stress (yield occurs first at the inner surface in both pore collapse and expansion). The yield threshold radius c is defined as the point at which the transition from an elastic to plastic state occurs, and is defined such that for $r \le c$, the stress state must equal the yield condition.

The transition from elastic-plastic to fully plastic deformation occurs when the yield threshold reaches the outer surface $(s_r(b) - s_\theta(b))$.

$$\alpha_c^{\mathbf{FP}} = \frac{2\alpha_0 G}{2G + Y} \tag{A.32}$$

The Carroll and Holt solution derives the elastic-plastic and fully plastic solutions from Eq. A.22. The presence of a pore fluid modifies only the p_a term. As with the elastic solution, we find that results with pore fluid are identical to those obtained for the hollow shell when the solution is expressed in terms of the effective stress.

In *pore collapse* we have (Carroll and Holt, 1972):

$$p_c^{\text{eff}}(\alpha) = \begin{cases} 4G(\alpha_0 - \alpha)/3\alpha(\alpha - 1), & \alpha_0 \geq \alpha \geq \alpha_c^{\mathbf{EP}} \\ \frac{2}{3}\left[G(2 - 2\alpha_0/\alpha) + \right. & \\ \left. Y \ln(\frac{2G(\alpha_0 - \alpha)}{Y(\alpha - 1)}) + Y\right], & \alpha_c^{\mathbf{EP}} > \alpha > \alpha_c^{\mathbf{FP}} \\ \frac{2}{3} Y \ln\left(\frac{\alpha}{\alpha - 1}\right), & \alpha_c^{\mathbf{FP}} \geq \alpha > 1 \end{cases} \tag{A.33}$$

Extending these results to *pore expansion*, we find that the elastic response is identical to the pore collapse solution. The yield stress in tension is $-Y$. Applying the same methodology, the resulting solution for pore expansion is:

$$p_e^{\text{eff}}(\alpha) = \begin{cases} 4G(\alpha_0 - \alpha)/3\alpha(\alpha - 1), & \alpha_0 \leq \alpha \leq \alpha_c^{\mathbf{EP}} \\ -\frac{4G}{3\alpha}(\alpha_0 - \alpha) & \\ -\frac{2Y}{3}\left[1 + \ln\left(\frac{2G(\alpha - \alpha_0)}{Y(\alpha - 1)}\right)\right], & \alpha_c^{\mathbf{EP}} < \alpha < \alpha_c^{\mathbf{FP}} \\ -\frac{2}{3} Y \ln\left(\frac{\alpha}{\alpha - 1}\right), & \alpha_c^{\mathbf{FP}} \leq \alpha \end{cases} \tag{A.34}$$

Where the transitions to elastic-plastic and fully-plastic deformation are:

$$\alpha_e^{\mathbf{EP}} = \frac{2\alpha_0 G - Y}{2G - Y} \tag{A.35}$$

$$\alpha_e^{\mathbf{FP}} = \frac{2\alpha_0 G}{2G - Y} \tag{A.36}$$

Appendix A.3. Porosity vs. Pressure

To generate the porosity vs. pressure curves in Fig. 2 and Fig. 3, the solution is expressed in terms of porosity (ϕ) rather than distension (α). The two are related by:

$$\alpha = \frac{1}{1 - \phi} \tag{A.37}$$

In terms of porosity rather than distension, the effective stress ($\bar{p}^{\text{eff}} = \bar{p}_b - \bar{p}_a$) for the *collapsing* spherical shell is:

$$p_c^{\text{eff}} = \begin{cases} \frac{4G}{3}\frac{(\phi_0 - \phi)(\phi - 1)}{\phi(\phi_0 - 1)}, & \phi_0 \geq \phi \geq \phi_c^{\mathbf{EP}} \\ \frac{2Y}{3}[\ln \frac{2G(\phi - \phi_0)}{Y\phi(\phi_0 - 1)} + 1] + \frac{4}{3}G\frac{\phi_0 - \phi}{\phi_0 - 1}, & \phi_c^{\mathbf{EP}} \geq \phi \geq \phi_c^{\mathbf{FP}} \\ -\frac{2Y}{3}\ln(\phi), & \phi_c^{\mathbf{FP}} \geq \phi \geq 0 \end{cases} \tag{A.38}$$

The transition from elastic to elastic-plastic ($\phi_c^{\mathbf{EP}}$), and elastic to fully-plastic ($\phi_c^{\mathbf{FP}}$) in pore collapse are

$$\phi_c^{\mathbf{EP}} = \frac{2G\phi_0}{2G + Y(1 - \phi_0)}, \tag{A.39}$$

and

$$\phi_c^{\mathbf{FP}} = \frac{2G\phi_0 + Y(\phi_0 - 1)}{2G}. \tag{A.40}$$

Similarly, for the *expanding* spherical shell:

$$p_e^{\text{eff}} = \begin{cases} \frac{4G}{3}\frac{(\phi_0 - \phi)(\phi - 1)}{\phi(\phi_0 - 1)}, & \phi_0 \leq \phi \leq \phi_c^{\mathbf{EP}} \\ \frac{2Y}{3}[\ln \frac{2G(\phi - \phi_0)}{Y\phi(\phi_0 - 1)} + 1] + \frac{4}{3}G\frac{\phi_0 - \phi}{\phi_0 - 1}, & \phi_c^{\mathbf{EP}} \leq \phi \leq \phi_c^{\mathbf{FP}} \\ -\frac{2Y}{3}\ln(\phi), & \phi_c^{\mathbf{FP}} \leq \phi \end{cases} \tag{A.41}$$

The transition from elastic to elastic-plastic ($\phi_e^{\mathbf{EP}}$), and elastic to fully-plastic ($\phi_e^{\mathbf{FP}}$) in expansion are

$$\phi_e^{\mathbf{EP}} = \frac{2G\phi_0}{2G + Y(\phi_0 - 1)}, \tag{A.42}$$

and

$$\phi_e^{\mathbf{FP}} = \frac{2G\phi_0 + Y(1 - \phi_0)}{2G}. \tag{A.43}$$

Appendix A.4. Pore Pressure

To generate the load-unload response plotted in Fig. 4, we first must express the porosity in terms of volumetric strain. We define the current and initial porosity in terms of the inner and outer shell radii:

$$\phi = a^3/b^3 \tag{A.44}$$

$$\phi_i = a_i^3/b_i^3 \tag{A.45}$$

The volumetric strain is defined in terms of the change in the outer shell radius

$$\varepsilon_v = \ln(b^3/b_i^3) \tag{A.46}$$

Since the matrix is incompressible the current and initial shell volumes must be equal.

$$(b^3 - a^4) = b_i^3 - a_i^3 \tag{A.47}$$

Combining Eq. A.44 through Eq. A.47 we obtain the following relations for switching between porosity and volumetric strain:

$$\phi = \mathbf{e}^{-\varepsilon_v}(\mathbf{e}^{\varepsilon_v} + \phi_i - 1) \tag{A.48}$$

$$\varepsilon_v = \ln(\frac{\phi_i - 1}{\phi - 1}) \tag{A.49}$$

Finally, the pore pressure depends on the change in pore volume, so

$$\overline{p}_f = K_f \ln(a_i^3/a^3) \tag{A.50}$$

Combining Eq. A.44 through Eq. A.50 the fluid pressure can be expressed in terms of current (ϕ) and initial porosity (ϕ_i).

$$\overline{p}_f = \begin{cases} K_f \ln\left(\frac{\phi_i(\phi - 1)}{\phi(\phi_i - 1)}\right), & \phi < \phi_i \\ 0, & \phi \geq \phi_i \end{cases} \tag{A.51}$$

Appendix A.5. Load-Unload Response

The initial porosity is only equal to the unloaded porosity (ϕ_0) when there is zero plastic strain in the matrix.

Setting $\bar{p} = \bar{p}_b = \bar{p}^{\text{eff}} + \overline{p}_f$, where $\bar{p}^{\text{eff}}$ is given by Eq. A.38 and Eq. A.41, and using $\bar{p}_a = \overline{p}_f$ from Eq. A.51 we obtain the porosity vs. pressure plots in Fig. 2 and Fig. 3.

The loading portion of Fig. 4 is obtained from Eq. A.38 and Eq. A.41 using the porosity-strain relation in Eq. A.48. To compute the unloading response, it is necessary to define a new *unloaded* porosity (different than the initial porosity). If the material has been compressed to some minimum porosity (ϕ^{min}), the new unloaded porosity (ϕ_0^{new}) is found by solving Eq. A.39.

$$\phi_0^{\text{new}} = \frac{2G\phi^{\text{min}} + Y}{2G + Y} \tag{A.52}$$

This new unloaded porosity is now used to evaluate Eq. A.38 and Eq. A.41, but the initial porosity is still used in Eq. A.51 and Eq. A.48.

For these plots, the following parameters were used.

Parameter	Description	Value
Y	Yield Strength (Compression)	414MPa
Y_t	Yield Strength (Tension)	75MPa
G	Shear Modulus	27GPa
ϕ_i	Initial Porosity	0.084
K_f	Fluid Bulk Modulus	2.2GPa
$\phi^{\min}$	Minimum Porosity	0.045

Appendix B. Penetration Simulation Parameters

Tables of constitutive model and simulation parameters.

Appendix B.1. Target Geometry

Parameters refer to the schematic in Fig. 8.

Parameter	Description	Value
t_f	Thickness of high res target face	5mm
l_c	Length of high res target core	50cm
l_t	Total target length	60cm
r_i	Core radius	2.5cm
r_o	Outer radius	5cm

Appendix B.2. Target Constitutive Model

Input parameters for the Arenisca constitutive model (Homel et al., 2014b).

Parameter	Feature	Value
ρ	Density (Drained)	2300kg/m^3
ρ	Density (Undrained)	2472kg/m^3
b_0	Bulk Modulus	1.003GPa
b_1	Bulk Modulus	14.7GPa
b_2	Bulk Modulus	41.0MPa
b_3	Bulk Modulus	1.0GPa
b_4	Bulk Modulus	4.0×10^{-3}
g_0	Shear Modulus	401.28MPa
g_1	Shear Modulus	0.25
g_2	Shear Modulus	−0.13
g_3	Shear Modulus	0.0
g_4	Shear Modulus	0.0
`FSLOPE`	Shear Limit Surface	0.435
`STREN`	Shear Limit Surface	100.0MPa
`YSLOPE`	Shear Limit Surface	0.079
`PEAKI1`	Shear Limit Surface	21.8457MPa
β	Nonassociativity	1.0
p_0	Crush Curve	−30MPa
p_1	Crush Curve	5.4×10^{-11}Pa^{-1}
p_2	Crush Curve	0.0
p_3	Crush Curve	0.189
CR	Cap Function	0.50
K_f	Pore Fluid	2.2GPa
$\bar{p}_f^i$	Pore Fluid	5.0MPa
T_1	Rate Dependence	4.0×10^{-4}s
T_2	Rate Dependence	0.835
n^{sub}	Subcycling	256

Appendix B.3. CVD jet description

Input parameters to described the CVD jet using the Arenisca constitutive model (Homel et al., 2014b). It is also necessary to define geometric objects and insertion rules to result in the desired velocity/density/radius profile along the length of the jet. The `Use_Disaggregation_Algorithm` flag will cause the model to define an initial material density based on the `void_fraction` defined for each geometric object.

Parameter	Feature	Value
ρ	Density (No Void)	19325kg/m^3
b_0	Bulk Modulus	268.7GPa
b_1	Bulk Modulus	0.0
b_2	Bulk Modulus	0.0
b_3	Bulk Modulus	0.0
b_4	Bulk Modulus	0.0
g_0	Shear Modulus	124.0GPa
g_1	Shear Modulus	0.0
g_2	Shear Modulus	0.0
g_3	Shear Modulus	0.0
g_4	Shear Modulus	0.0
`FSLOPE`	Shear Limit Surface	0.0
`STREN`	Shear Limit Surface	404.0MPa
`YSLOPE`	Shear Limit Surface	0.0
`PEAKI1`	Shear Limit Surface	0.0
β	Nonassociativity	1.0×10^{-3}
p_0	Crush Curve	−100kPa
p_1	Crush Curve	1.0×10^{-5}Pa^{-1}
p_2	Crush Curve	0.0
p_3	Crush Curve	0.5
CR	Cap Function	0.09
K_f	Pore Fluid	0.0
$\bar{p}_f^i$	Pore Fluid	0.0
T_1	Rate Dependence	0.0
T_2	Rate Dependence	0.0
n^{sub}	Subcycling	256
	Disaggregation	`true`